

APPENDIX A: INDIVIDUAL RESULTS

A1 HE 0020-1741

Figure A1 shows our results for HE 0020-1741, an ultra metal-poor star studied by [Placco et al. \(2016\)](#). Even if the parallax from Gaia DR2 has a large uncertainty ($\varpi = 0.1456 \pm 0.0384$ mas; red solid line for the MW halo prior and a red dot-dashed line for the disc+halo prior in the top-left pane), it is enough to break the dwarf/giant degeneracy obtained from the photometric solution (black line). The final PDFs are shown, using the MW halo prior and the disc+halo prior, respectively as the solid blue and the dot-dashed blue curves in that panel and, in both cases, the final scenario is a giant located at 10.3 ± 0.4 kpc. The stellar parameters we infer are in agreement with the values from the literature. In the lower panels of Figure A1, both the orbits calculated from the inferred distances from the PDF and Gaia astrometry only are shown, respectively marked by the blue and the red lines. The orbital parameters relative to the distance PDF represent an unbound orbit, while the Gaia astrometric distance leads to a more benign orbit that remains in the inner part of the MW halo.

A2 SDSS J0023+0307

Figure A2 summarises our results for SDSS J0023+0307, which is a mega metal-poor star found by [Aguado et al. \(2018a\)](#). The Gaia parallax is not very informative ($\varpi = 0.2697 \pm 0.1406$ mas; red solid line for the MW halo prior and a red dot-dashed line for the disc+halo prior in the top-left panel) and cannot break the dwarf/giant degeneracy inherent to the photometric solution (black line). It is nevertheless entirely compatible with that inference. The final PDFs are shown, using the MW halo prior and the disc+halo prior, respectively as the solid blue and the dot-dashed blue curves in that panel and, in both cases, yields a more likely dwarf solution at 2.71 ± 0.14 kpc along with a less likely sub-giant solution at 11.03 ± 0.73 kpc. The stellar parameters we infer for the most likely dwarf solution are entirely compatible with the literature values. Combined with the exquisite Gaia proper motions, the two distance solutions yield drastically different orbits. The sub-giant distance peak implies an unbound orbit that is shown in orange, while the (more likely) dwarf solution produces a more benign orbit that remains within the inner MW (shown in blue), supporting the distance of the latter solution as the valid one. While eccentric, this orbit surprisingly remains confined close to the MW plane ($|Z| < 5.0$ kpc).

A3 HE 0044-3755

HE 0044-3755 is an ultra metal-poor star studied by [Cayrel et al. \(2004\)](#) and our results for this star are shown in Figure A3. The distance PDF constrains the distance to 5.70 ± 0.25 kpc. This result leads to a giant solution that is compatible with the values in the literature. The orbit of this star is typical of a halo star.

A4 HE 0057-5959

Our results for HE 0057-5959 are shown in Figure A4, taking the literature values from [Norris et al. \(2013\)](#). From the distance PDF, we see a disagreement between the photometric and the astrometric likelihoods, which we cannot trace to any obvious source, but the astrophysical parameter inference is compatible with the literature values. For this giant, we show the orbit inferred both from our full astrometric and photometric analysis (blue orbit) and when using only the Gaia astrometry with the MW prior (red orbit). In both cases, HE 0057-5959 remains in the inner region of the MW halo (apocentre < 30 kpc).

A5 HE 0107-5240

HE 0107-5240 is likely a binary system ([Arentsen et al. 2018](#)) discovered by radial velocity variation. Its spectrum does not present double lines indicating that the light is not polluted by the secondary. It is a hyper metal-poor star analysed by [Christlieb et al. \(2004\)](#). Our results are shown in Figure A5 and we infer a distance of 14.3 ± 1.0 kpc, corresponding to the giant solution because the probability of the dwarf solution is entirely suppressed by the Gaia parallax information. Our values for surface gravity and effective temperature are in perfect agreement with the literature values. The orbit of this star is typical of an eccentric halo orbit and remains within $15.9^{+1.0}_{-0.9}$ kpc.

A6 HE 0134-1519

Our analysis of HE 0134-1519 ([Hansen et al. 2015](#)) is shown in Figure A6. This is another case for which the astrometric and photometric likelihoods disagree, yielding very different orbits, even though it is clear this star is a giant, in agreement with the literature. Both orbital solutions are indicative of a halo star, but the closer Gaia-only distance solution yields an orbit that remains much closer to the Galactic center (apocentre of $25.7^{+4.6}_{-1.7}$ kpc vs. $70.2^{+49.3}_{-20.7}$ kpc).

A7 SDSS J014036.21+234458.1

For the dwarf star SDSS J014036.21+234458.1 ([Yong et al. 2013](#), Figure A7), the astrometric and photometric distances are technically in disagreement, but the distance inferences are so similar that it does not impact our results. We infer a distance of 0.76 ± 0.02 kpc and an orbit that brings SDSS J014036.21+234458.1 close to the MW plane ($|Z| < 2.5$ kpc).

A8 BD+44 493

Our results for BD+44 493 ([Ito et al. 2013](#), Figure A8) are strongly constrained by the exquisite Gaia parallax, yielding a distance of 0.211 ± 0.003 kpc. Just like with SDSS J0023+0307, this star is eccentric and stays extremely close to the MW plane ($|Z| < 1.5$ kpc). It has an apocentre at the Solar circle.

A9 HE 0233-0343

The combined astrometric and photometric analysis of HE 0233-0343 (Hansen et al. 2015, Figure A9) yields an accurate distance of 1.09 ± 0.04 kpc. Despite this, our $\log(g)$ inference is incompatible with the literature value, but the very accurate Gaia parallax lends support to our inference. Like the previous star, HE 0233-0343 remains confined to the region of the MW disc, with $|Z| < 2.6$ kpc and an apocentre of $11.9^{+0.5}_{-0.4}$ kpc.

A10 BPS CS 22963-0004

For this UMP studied by Roederer et al. (2014), we infer a distance of 4.5 ± 0.4 kpc (Figure A10). Our astrophysical parameter inference disagrees with the literature values but the MESA isochrones strongly constrain our temperature inference. The difference could hint at systematics in these isochrones or the Roederer et al. (2014) analysis. Despite the currently proximity to this star, its orbit brings it very far into the MW halo, with $r_{\text{apo}} = 155.8^{+183.4}_{-55.0}$ kpc.

A11 SDSS J030444.98+391021.1

The Gaia parallax of SDSS J030444.98+391021.1 (Aguado et al. 2017b, Figure A11) is very uncertain ($\varpi = 0.0752 \pm 0.1929$ mas) but, in case of the halo prior, strongly suppresses the dwarf solution (1% of the PDF). However, the orbital analysis shows that the favoured giant scenario implies that this star is not bound to the MW. According to this, we repeat the analysis with the disc+halo prior finding that the inferred distances are not significantly changed but the fractional probability of the peaks is. With this prior, the dwarf solution represents 21% of the PDF. Taking into account the orbital analysis, the dwarf solution appears to be the more realistic distance estimate (1.51 ± 0.07 kpc). This solution is also compatible with the $\log(g)$ of Aguado et al. (2017b), contrary to the result from the giant solution. We note that a slightly larger distance for the dwarf solution would be entirely compatible with the Gaia parallax and we think that the low likelihood of the dwarf solution could be driven further down than it should by a systematic in the models we use. With our favoured close-by distance, this star has the orbit of an inner halo object.

A12 SMSS J031300.36-670839.3

For this star with the lowest iron-abundance ($[\text{Fe}/\text{H}] < -6.53$, Nordlander et al. 2017, Figure A12), we infer a distance of 12.0 ± 0.8 kpc corresponding to the giant solution ($\log(g) = 1.8 \pm 0.1$). The literature $\log(g)$ is however in better agreement with the Gaia-only distance that is a little closer. The orbital analysis implies that this star has a fairly eccentric orbit and that, using the Gaia-only distance, it is compatible with an inner halo object. With the final posterior, we infer an outer halo orbit.

A13 HE 0330+0148

As we can see in Figure ??, the analysis fails for this carbon-enhanced star (also known as G77-61) and its location in the colour-magnitude diagram does not coincide with the

isochrone models. The strong carbon bands dominate in the spectrum (Dahn et al. 1977), where the Gaia DR2 BP filter is sensitive, leading to an abnormal value of $(BP - RP)$ colour and, as a consequence, this star lays outside the isochrone range. This could also explain the strong disagreement between the photometric-only and astrometric-only distance likelihood functions (see Figure A13). We don't think that the binarity can affects the photometry because the companion is most likely an unseen white dwarf with a period of 250 days (Dearborn et al. 1986), which means that the Gaia DR2 magnitudes correspond to the magnitude of the star itself and not that of the binary system. In this case, we favour the Gaia-only inference with 78 ± 1 pc. HE 0330+0148 has a very radial orbit and its current position near the Sun is near its apocentre. Its orbit is close to the MW plane ($|Z| < 2.8$ kpc).

A14 HE 0557-4840

The inferred result on HE 0557-4840 (Norris et al. 2007, Figure A14) shows it is a giant halo star at a distance of 20.0 ± 1.3 kpc. Although the peaks of the astrometric and photometric solutions are shifted by ≈ 6 kpc, these are compatible due to the Gaia parallax that is poorly constrained ($\varpi = 0.0389 \pm 0.0207$ mas).

A15 SDSS J081554.26+472947.5

Our results on SDSS J081554.26+472947.5 (Aguado et al. 2018b, Figure A15) show that the star is a dwarf that is located at a distance of 1.59 ± 0.07 kpc and orbits within the inner halo. Our stellar parameter inference is in agreement with the literature values.

A16 SDSS J092912.32+023817.0

The distance PDF for this star (Bonifacio et al. 2015; Cafau et al. 2016, Figure A16) shows two solutions that are not strongly constrained due to the non-informative Gaia parallax ($\varpi = 0.1276 \pm 0.1872$ mas). Using a MW halo prior, the sub-giant scenario has a greater likelihood (68% vs. 32%), but it yields an orbit that is not bound to the MW. We therefore reanalyse this star using a disc+halo orbit, finding that the dwarf solution is now preferred (95% vs. 5%). Hence, this star is located at a distance of 2.4 ± 0.2 kpc (dwarf solution) and its orbit is perpendicular to the disc with $r_{\text{apo,dwarf}} = 23.5^{+2.6}_{-1.4}$ kpc.

A17 SDSS J094708.27+461010.0

The distance to SDSS J094708.27+461010.0 is not constrained by the Gaia parallax ($\varpi = 0.1989 \pm 0.2299$ mas, Aguado et al. 2017a, Figure A17). However, for similar reasons to those mentioned above, we favour the dwarf scenario (distance of 3.8 ± 0.3 kpc) as a larger distance would mean that this star is not bound to the MW. The orbital analysis shows that its orbital plane is perpendicular to the MW plane.

A18 HE 1012-1540

For HE 1012-1540 (Roederer et al. 2014, Figure A18), the combination of photometric likelihood and the exquisite Gaia parallax leads to a distance of 0.384 ± 0.004 kpc and strongly implies that this is a dwarf star. It is worth noting that the inferred stellar parameters are not in agreement with the literature in which the giant solution is preferred, but the latter seems hardly compatible with the strongly constrained distance. The orbit of this star implies that it remains confined close to the MW plane but has a high eccentricity ($\epsilon = 0.83^{+0.00}_{-0.01}$).

A19 SDSS J102915+172927

SDSS J102915+172927, which is currently the most metal-poor star known (Caffau et al. 2011), is presented in Figure A19. The dwarf solution from the photometric likelihood is in agreement with the Gaia parallax and yields a well-constrained distance of 1.28 ± 0.05 kpc. We infer a higher surface gravity than in the literature, but our effective temperature inference is compatible. The orbital analysis shows that this star has the orbit of a disc star with an almost circular orbit around the galactic centre ($\epsilon = 0.12^{+0.01}_{-0.01}$) that remains close to the MW plane ($|Z| < 2.3$ kpc). These orbital properties differ from but supersede those of Caffau et al. (2012) that were based on PPMXL Catalogue for proper motions (Roeser, Demleitner & Schilbach 2010, $\mu_\alpha = -12.8 \pm 3.9$ mas/yr and $\mu_\delta = -6.7 \pm 3.9$ mas/yr).

A20 SDSS J103402.70+070116.6

Our results for SDSS J103402.70+070116.6 (Bonifacio et al. 2018) are shown in Figure A20 and, as we can see, the Gaia parallax does not allow us to break the dwarf/sub-giant degeneracy ($\varpi = 0.2874 \pm 0.1367$ mas). The dwarf solution ($P_{\text{dwarf}} = 89\%$ vs. $P_{\text{giant}} = 11\%$) at 2.79 ± 0.26 kpc implies an eccentric orbit ($\epsilon = 0.63^{+0.03}_{-0.04}$) that remains confined to the Galactic plane ($|Z| < 2.7$ kpc). On the other hand, the subgiant solution at 8.3 ± 0.6 kpc brings that star further out in the halo $r_{\text{apo}} = 24.3^{+17.8}_{-0.0}$ kpc. Repeating the analysis with the disc+halo prior, the two new solutions are in agreement within the uncertainties with previous results, but now the sub-giant scenario is strongly suppressed (0.6%).

A21 SDSS J103556.11+064143.9

For this star (Bonifacio et al. 2015), the Gaia parallax is negative and does not help to constrain the distance ($\varpi = -0.3912 \pm 0.3163$ mas). Our analysis implies that the dwarf solution at 3.97 ± 0.34 kpc is more likely and this is confirmed by the orbital analysis that yields a large value for the apocentre in case of the giant solution ($r_{\text{apo}} = 147.8^{+25.5}_{-11.8}$ kpc). Just like with SDSS J103402.70+070116.6 above, the literature $\log(g)$ falls in-between the two solutions we obtain and only the effective temperature inference is compatible with the literature.

A22 SDSS J105519.28+232234.0

The distance PDF for this star (Aguado et al. 2017b, Figure A22) indicates a strongly preferred distance of $3.49 \pm$

0.45 kpc corresponding to the dwarf solution, with the effective temperature in agreement with the literature. The inferred orbital parameters indicate an inner halo orbit.

A23 SDSS J120441.38+120111.5

The analysis on this star (Placco et al. 2015, Figure A23) leads to the conclusion that this star is a subgiant located at a distance of 7.03 ± 0.54 kpc from the Sun with an inner halo-like orbit.

A24 SDSS J124719.46-034152.4

The Gaia parallax on this star is poorly constraining ($\varpi = 0.3075 \pm 0.2098$ mas, Figure A24) and, combined with the photometric likelihood, we obtain a favoured distance of 4.17 ± 0.32 kpc corresponding to the dwarf solution that has an inner halo orbit. The far less likely sub-giant solution yields an orbit that is not bound to the MW. For the stellar parameters, the inferred effective temperature is compatible with the literature value (Caffau et al. 2013b).

A25 LAMOST J125346.09+075343.1

Figure A25 shows our results for LAMOST J125346.09+075343.1 (Li et al. 2015) and, as we can see, the Gaia likelihood is not in agreement with the photometric one. Our combined distance analysis favours the sub-giant scenario and a distance of 0.766 ± 0.016 kpc, which is close to the Gaia-only inference (0.698 ± 0.018 kpc). The surface gravity we infer is compatible with the value in the literature but our analysis implies a hotter star. Both the orbits from Gaia and the distance PDF show that LAMOST J125346.09+075343.1 remains confined to the MW plane, even though it has a high eccentricity ($\epsilon = 0.75^{+0.03}_{-0.02}$).

A26 SDSS J131326.89-001941.4

The Gaia parallax for this object is poorly constraining ($\varpi = 0.2976 \pm 0.0972$ mas, Figure A26) and we obtain using a pure halo prior that the preferred solution, a giant ($> 99\%$ chance), is located at the distance of 8.6 ± 2.9 kpc, with the inferred stellar parameters that are in agreement with the literature (Allende Prieto et al. 2015; Frebel et al. 2015; Aguado et al. 2017b). From the orbital analysis, this star is classifiable as inner halo.

A27 HE 1310-0536

The Gaia parallax ($\varpi = 0.0078 \pm 0.0342$ mas) rules out the dwarf solution for HE 1310-0536 (Figure A27; Hansen et al. 2015) and we infer a distance of 20.6 ± 0.9 kpc. The inferred stellar parameters are not in agreement with the literature, but this could stem from systematics in the red-giant-branch part of the isochrones we rely on. The orbit of this star clearly brings it in the outer parts of the halo, with $r_{\text{apo}} = 99.7^{+38.3}_{-26.0}$ kpc.

A28 HE 1327-2326

The results for HE 1327-2326 are shown in Figure A28, and, despite the fact that the Gaia and the photometric likelihoods are not in good agreement, the sub-giant scenario is clearly favoured. The distance obtained for the combined analysis is 1.21 ± 0.02 kpc (or 1.09 ± 0.03 kpc for the Gaia only analysis) and the inferred effective temperature deviates somewhat from the literature value (Frebel et al. 2008). Even though the combined and Gaia-only distances yield significantly different orbits, they both imply halo orbits.

A29 HE 1424-0241

This giant star is located at a distance of 10.3 ± 1.0 kpc (Figure A29) and the inferred stellar parameters are in agreement with the literature (Cohen et al. 2008; Norris et al. 2013). The orbital analysis shows that HE 1424-0241 has an inner-halo orbit with high a eccentricity ($\epsilon = 0.81^{+0.06}_{-0.09}$).

A30 SDSS J144256.37-001542.7

The distance PDF for the combined analysis of SDSS J144256.37-001542.7 (Caffau et al. 2013a; Figure A30) still shows two peaks because of the poorly constraining Gaia parallax ($\varpi = -0.3910 \pm 0.2981$ mas). The giant solution and its distance of 11.3 ± 1.0 kpc is the preferred one with a halo prior ($P_{\text{giant}} = 87\%$ vs. $P_{\text{dwarf}} = 13\%$) but implies an unbound orbit whereas the dwarf solution at 2.68 ± 0.27 kpc yields a more benign halo orbit with $r_{\text{apo}} = 39.1^{+5.2}_{-2.6}$ kpc. Similar distances are found with a disc+halo prior but with the dwarf solution as preferred scenario ($P_{\text{dwarf}} = 84\%$ vs. $P_{\text{giant}} = 16\%$).

A31 Pristine 221.8781+9.7844

The small Gaia parallax of Pristine 221.8781+9.7844 (Starkenburg et al. 2018; $\varpi = 0.1187 \pm 0.0940$ mas) rules out the dwarf solution. Hence the final picture of a sub-giant located at 7.36 ± 0.55 kpc from the Sun. As we can see from Figure A31, the inferred stellar parameters agree with the literature and the orbit we infer for Pristine 221.8781+9.7844 indicate that this star has a halo orbit almost perpendicular to the MW plane.

A32 SDSS J164234.48+443004.9

SDSS J164234.48+443004.9 (Figure A32) is a dwarf star located at a distance of 2.66 ± 0.16 kpc (Figure A32). The stellar parameters are compatible with the literature values (Aguado et al. 2016). The orbital analysis suggests that this star remains confined to the MW plane, but has a high eccentricity ($\epsilon = 0.72^{+0.03}_{-0.04}$).

A33 SDSS J173403.91+644633.0

SDSS J173403.91+644633.0 has a non-informative Gaia parallax ($\varpi = -0.1052 \pm 0.2702$ mas) that does not break the dwarf/giant degeneracy (Figure A33). The dwarf solution with a distance of 5.46 ± 1.02 kpc is nevertheless strongly

preferred by the photometric analysis and yields a more realistic inner halo orbit that remains bound to the MW, contrary to the giant solution. The inferred stellar parameters are in agreement with those from the Aguado et al. (2017a) analysis.

A34 SDSS J174259.67+253135.8

Similarly to the previous star, the Gaia parallax of SDSS J174259.67+253135.8 ($\varpi = -0.1628 \pm 0.1870$ mas) does not allow us to discriminate between the dwarf and giant solutions but the giant solution implies an orbit with a very large apocentre beyond 700 kpc and we therefore favour the dwarf solution at 4.46 ± 0.52 kpc (Figure A34). With this distance, SDSS J174259.67+253135.8 (Bonifacio et al. 2015) is on an eccentric orbit that remains close to the MW plane ($|Z| < 2.7$ kpc).

A35 2MASS J18082002-5104378

Schlaufman, Thompson & Casey (2018) show that this star is in a binary system. The orbital parameters they derive show that this binary system has a very low eccentric orbit and is confined to the MW plane ($|Z| < 0.13$ kpc). From our distance analysis, the photometric likelihood is not in agreement with the exquisite Gaia parallax ($\varpi = 1.6775 \pm 0.0397$ mas), but we derive a similar overall solution at a distance of 0.647 ± 0.012 kpc and stellar parameters in agreement with the literature values (Meléndez et al. 2016, Figure A35). In agreement with the work from Schlaufman, Thompson & Casey (2018), we derive that the orbit is very close to the MW plane and even confined inside the thin disc ($|Z| < 0.166$ kpc) with a very low eccentricity of $\epsilon = 0.090^{+0.006}_{-0.005}$.

A36 BPS CS 22891-0200

The PDF of BPS CS 22891-0200 (Roederer et al. 2014; Figure A36) shows that is a giant star near the tip (see also Figure ??), located at the distance of 14.7 ± 0.5 kpc. Our inferred stellar parameters do not match the values from the literature. The orbit of BPS CS 22891-0200 brings it far out into the halo of the MW ($r_{\text{apo}} = 64.0^{+18.9}_{-11.1}$ kpc).

A37 BPS CS 22885-0096

Figure A37 presents our results for BPS CS 22885-0096 (Roederer et al. 2014), indicating that it is a giant at a distance of 6.65 ± 0.22 kpc, even though the stellar parameters we infer differ from the literature values. The orbit of this star is confined to a very narrow plane that is perpendicular to the MW plane.

A38 BPS CS 22950-0046

The Gaia parallax for this star ($\varpi = 0.0587 \pm 0.0270$ mas) clearly rules out the dwarf solution (Figure A38). As the plots show, this halo giant star is at a distance of 19.1 ± 0.3 kpc and the inferred stellar parameters are not in agreement with the literature (Roederer et al. 2014).

A39 BPS CS 30336-0049

Figure A39 shows that BPS CS 30336-0049 is located at 15.5 ± 0.7 kpc and follows an orbit that brings it far into the MW halo ($r_{\text{apo}} = 122.7^{+51.1}_{-41.4}$ kpc). The inferred effective temperature matches the value from the literature (Lai et al. 2008), while our constraints on the gravity yields a slightly lower $\log(g)$.

A40 HE 2139-5432

Our results on HE 2139-5432 are summarised in Figure A40, and they lead to the conclusion that this star is a giant located at a distance of 11.0 ± 0.9 kpc from the Sun. The inferred surface gravity is in agreement with the literature (Norris et al. 2013) but the effective temperature is slightly cooler. The inferred orbit indicates that HE 2139-5432 is an inner halo star with a high eccentricity ($e = 0.79^{+0.05}_{-0.06}$).

A41 HE 2239-5019

For this star, the photometric and the astrometric likelihoods are in agreement, indicating the subgiant scenario at 4.19 ± 0.28 kpc is the valid solution (Figure A41). The orbit of HE 2239-5019 brings it at fairly large distances in the halo, with $r_{\text{apo}} = 52.9^{+16.6}_{-10.4}$ kpc. The inferred surface gravity and effective temperature are compatible with the values from literature (Hansen et al. 2015).

A42 HE 2323-0256

Although the Gaia parallax is uncertain ($\varpi = 0.0038 \pm 0.0359$ mas), it helps break the dwarf/giant degeneracy. The final solution is that of a giant at a distance of 14.2 ± 0.6 kpc, belonging to the halo (Figure A42). We obtain higher values for the effective temperature and surface gravity than Roederer et al. (2014).

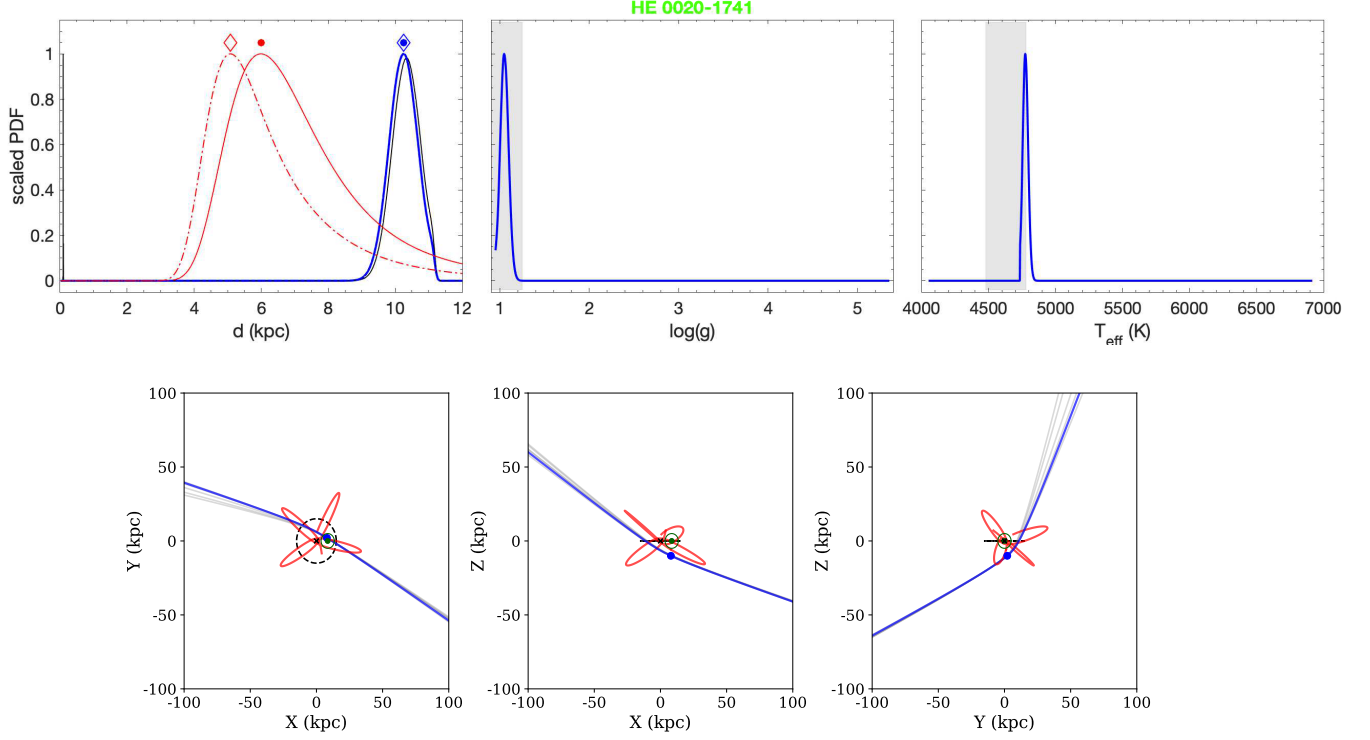


Figure A1. Left top: posterior probability (blue solid line and blue dot-dashed line respectively using a halo and a disc+halo prior), photometric likelihood (black line), and the product between the astrometric likelihood and MW prior (red solid line and red dot-dashed line respectively using a halo and a disc+halo prior) as a function of distance for HE 0020-1741. The coloured dots and the diamonds represent the position of the maxima of their same colour distribution respectively using a halo and a disc+halo prior. Center top: posterior probability as a function of $\log(g)$ (blue solid line for MW halo prior and blue dash-dot line for disc+halo prior). The gray box represents the surface gravity from literature within 1σ . Right top: posterior probability as a function of T_{eff} (blue solid line for MW halo prior and blue dot-dashed line for disc+halo prior). The gray box represents the effective temperature from literature within 1σ . The PDFs are rescaled to 1. Bottom panels: Blue and red lines are, respectively, the projected orbits of HE 0020-1741 for the most probable distance from PDF and for the distance from Gaia astrometric only inference in the plane YX (left), ZX (center) and ZY (right). The Galactic plane within 15 kpc (black line) and the Sun (green dot) are shown. Gray orbits represent randomisations around the values of position, distance, radial velocity and proper motions.

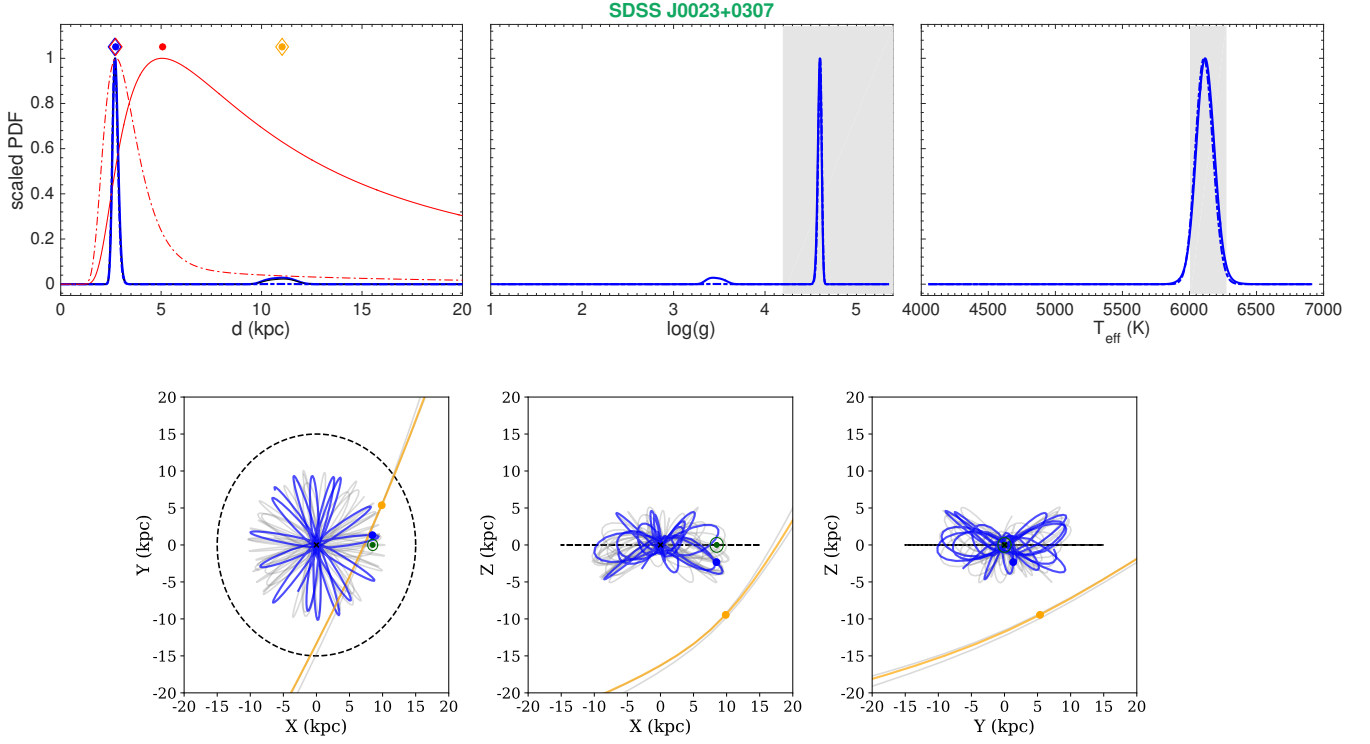


Figure A2. Left top: posterior probability (blue solid line and blue dot-dashed line respectively using a halo and a disc+halo prior), photometric likelihood (black line), and the product between the astrometric likelihood and MW prior (red solid line and red dot-dashed line respectively using a halo and a disc+halo prior) as a function of distance for SDSS J0023+0307. The coloured dots and the diamonds represent the position of the maxima of their same colour distribution respectively using a halo and a disc+halo prior. Center top: posterior probability as a function of $\log(g)$ (blue solid line for MW halo prior and blue dash-dot line for disc+halo prior). The gray box represents the surface gravity from literature within 1σ . Right top: posterior probability as a function of T_{eff} (blue solid line for MW halo prior and blue dot-dashed line for disc+halo prior). The gray box represents the temperature from literature within 1σ . The PDFs are rescaled to 1. Bottom panels: Blue and orange lines are, respectively, the projected orbits of SDSS J0023+0307 for the most probable distance and for the second peak in the distance posterior in the plane YX (left), ZX (center) and ZY (right). The Galactic plane within 15 kpc (black line) and the Sun (green dot) are shown. Gray orbits represent randomisations around the values of position, distance, radial velocity and proper motions.

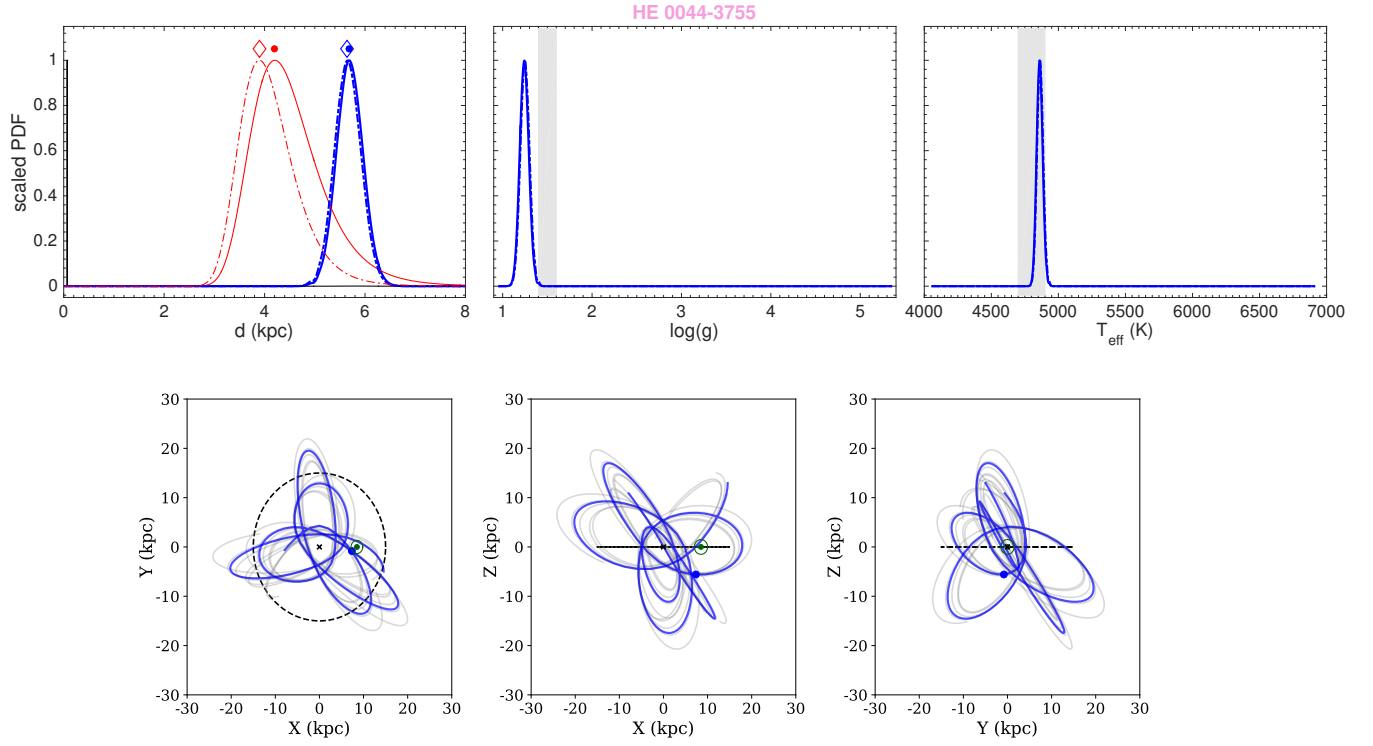


Figure A3. Same as Figure A2, but for HE 0044-3755.

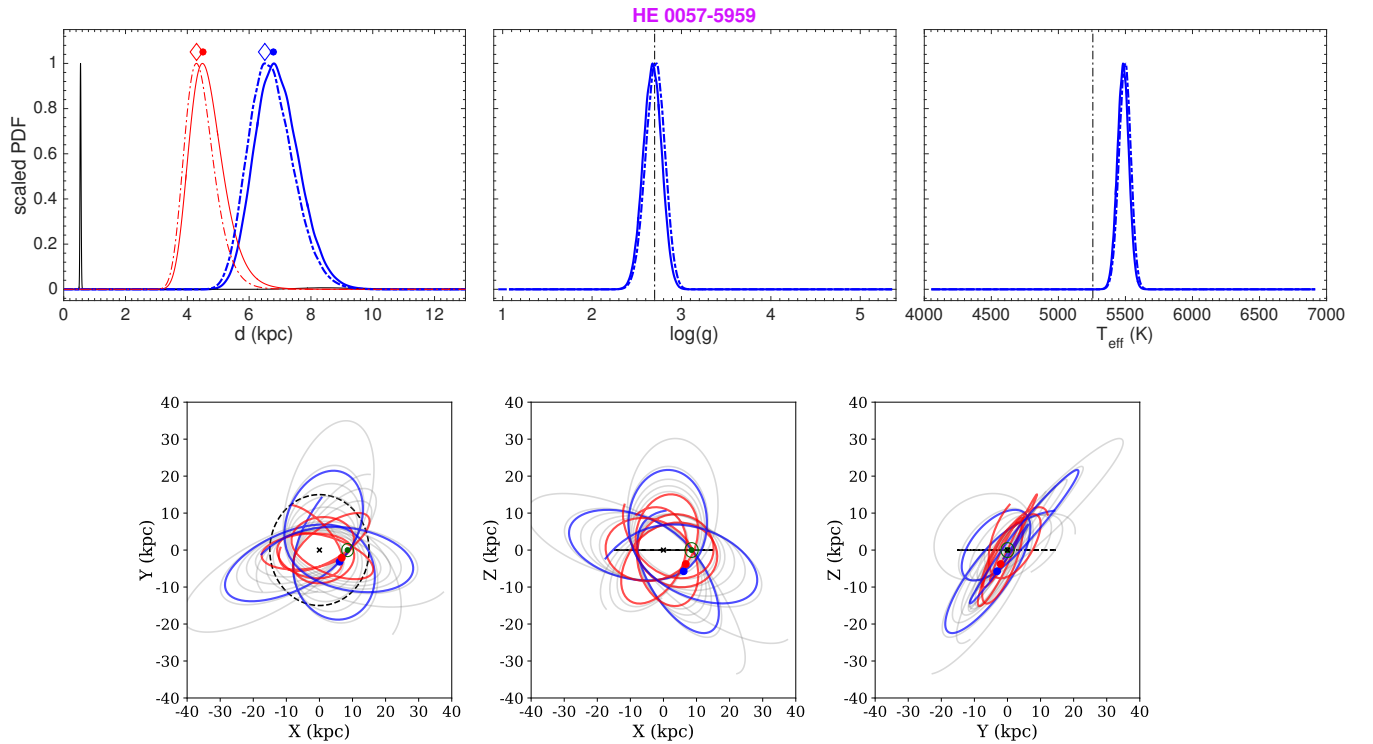


Figure A4. Same as Figure A2, but for HE 0057-5959. For this star, the orbit inferred from the product between the astrometric likelihood and MW halo prior is shown with the red line.

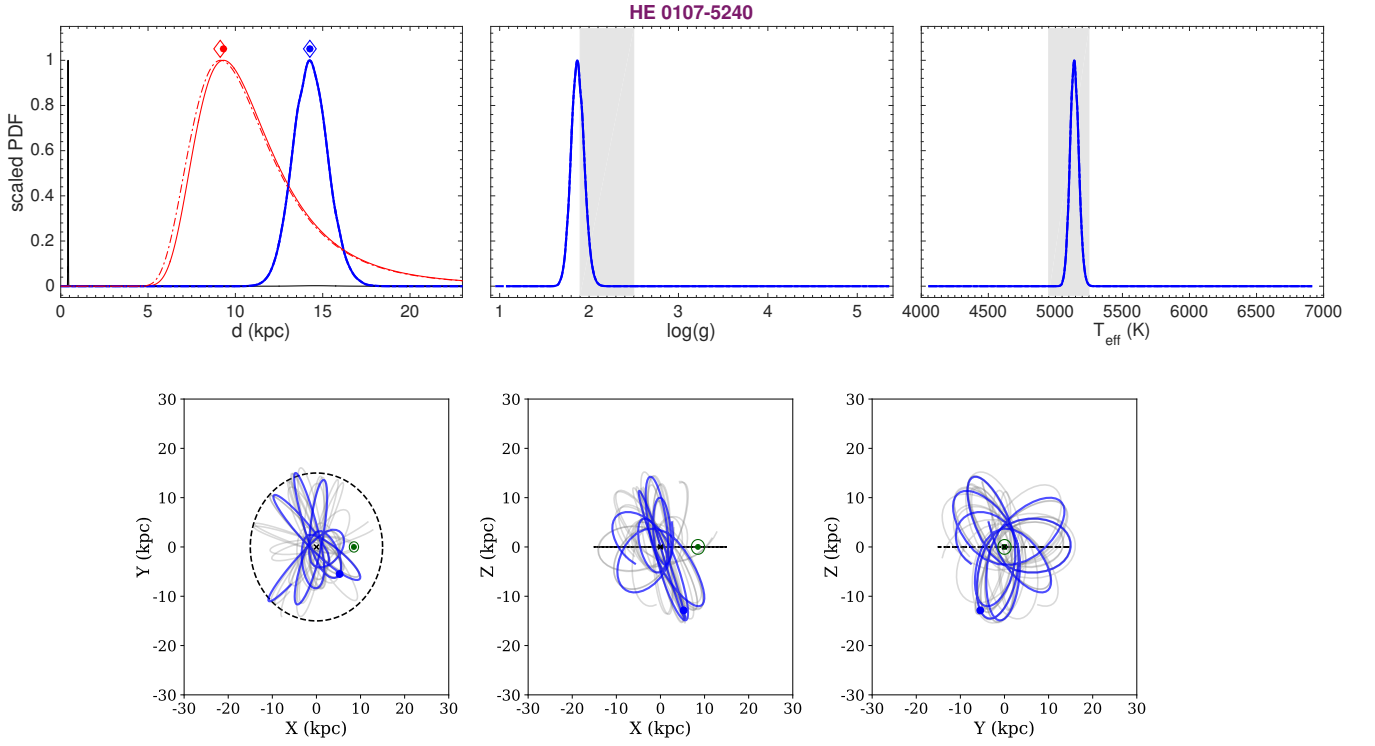


Figure A5. Same as Figure A2, but for HE 0107-5240.

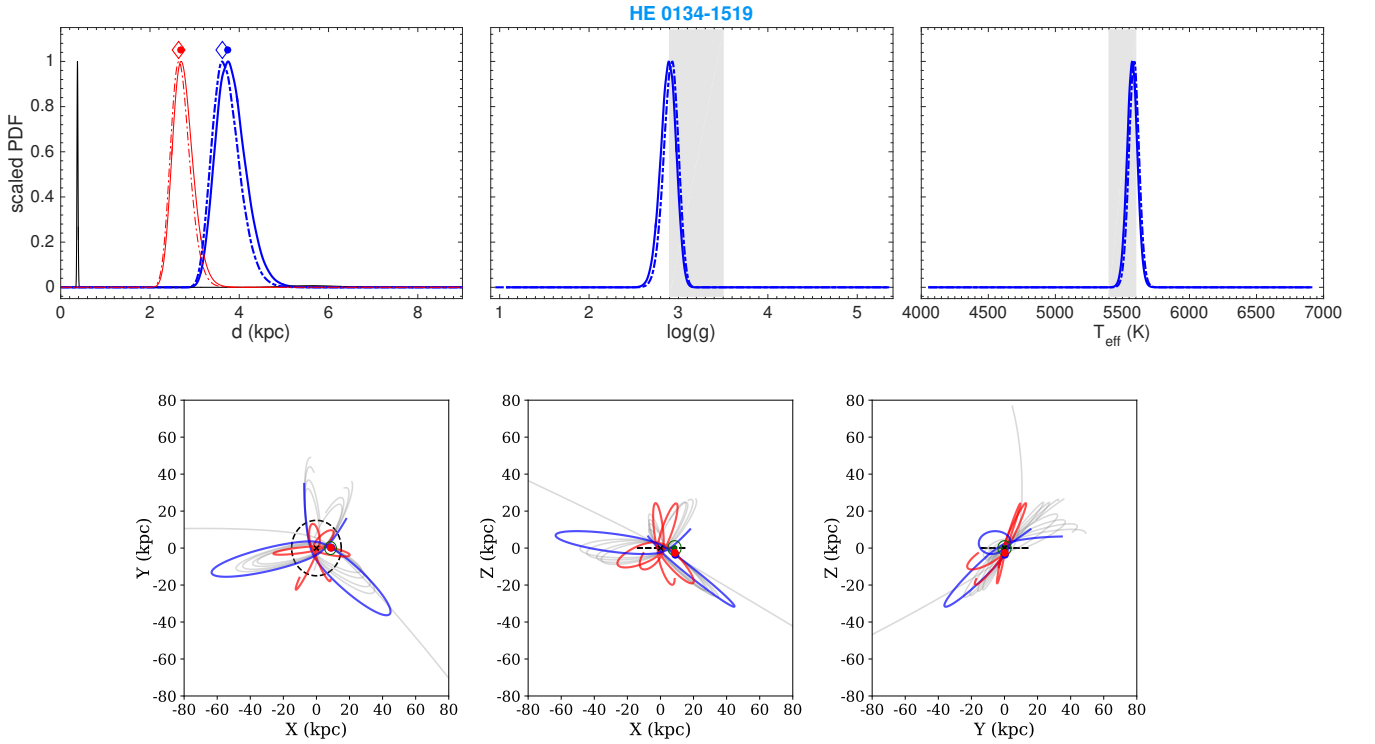


Figure A6. Same as Figure A2, but for HE 0134-1519. For this star, the orbit inferred from the product between the astrometric likelihood and MW halo prior is shown with the red line.

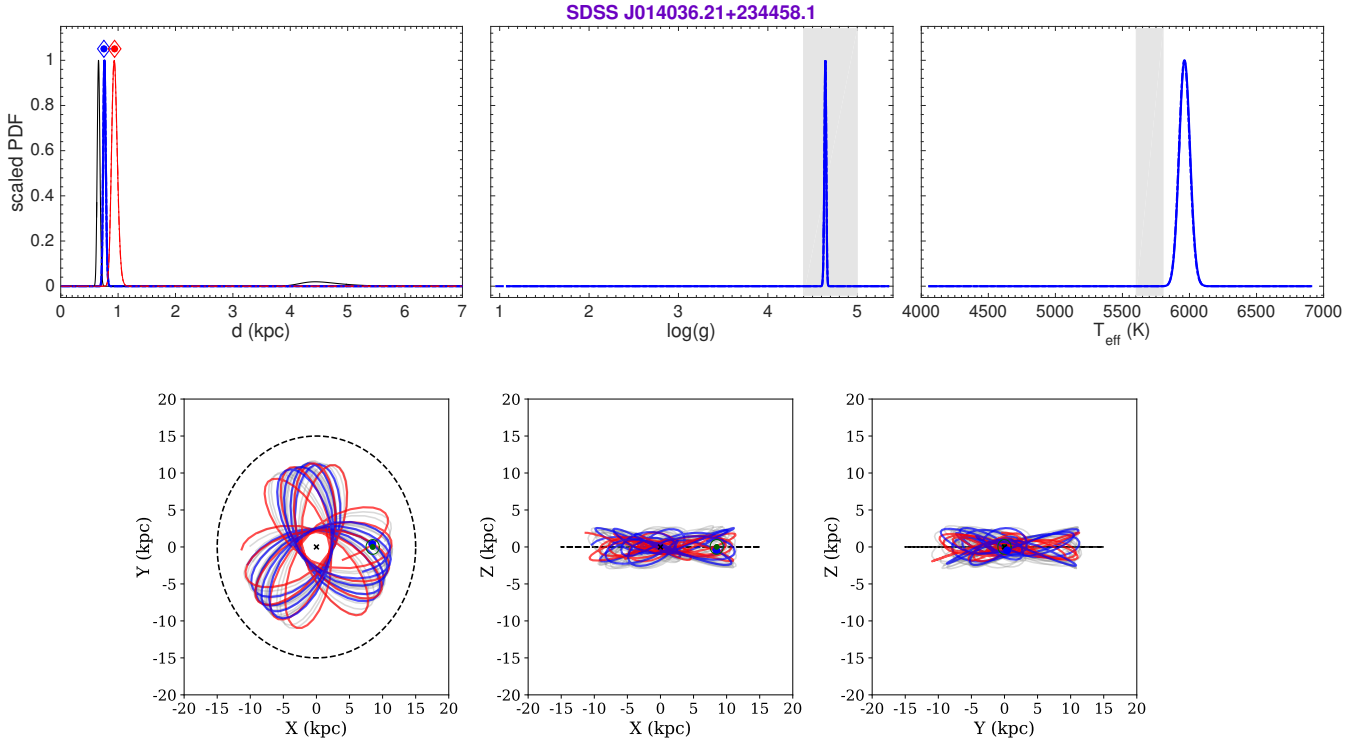


Figure A7. Same as Figure A2, but for SDSS J014036.21+234458.1. For this star, the orbit inferred from the product between the astrometric likelihood and MW halo prior is shown with the red line.

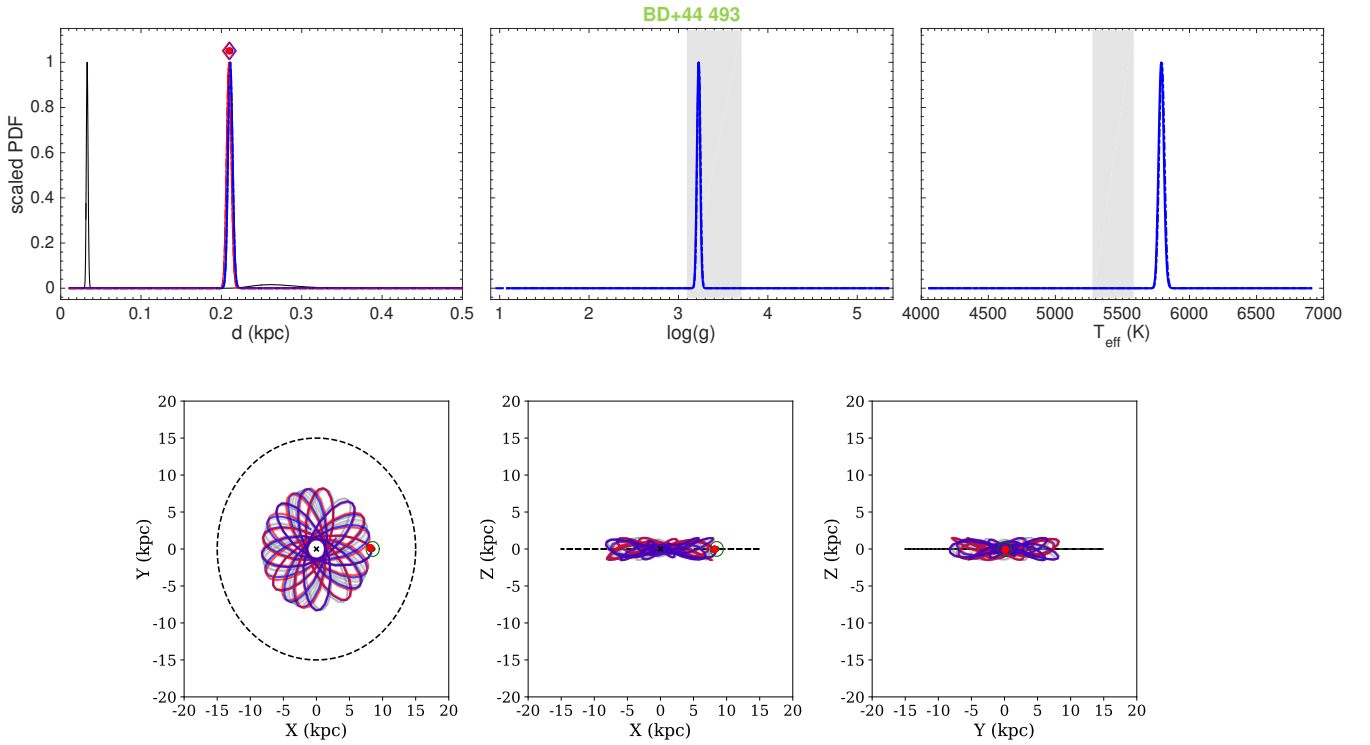


Figure A8. Same as Figure A2, but for BD+44 493. For this star, the orbit inferred from the product between the astrometric likelihood and MW halo prior is shown with the red line.

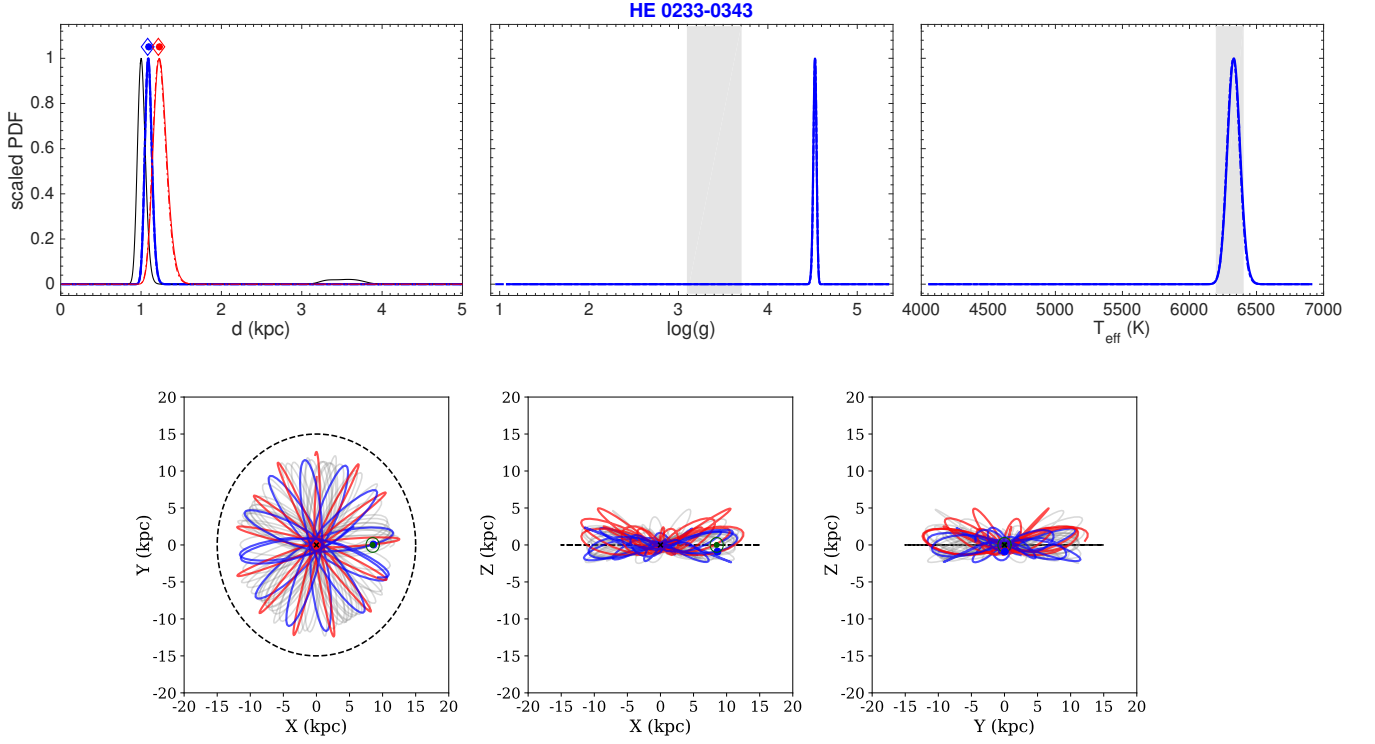


Figure A9. Same as Figure A2, but for HE 0233-0343. For this star, the orbit inferred from the product between the astrometric likelihood and MW halo prior is shown with the red line.

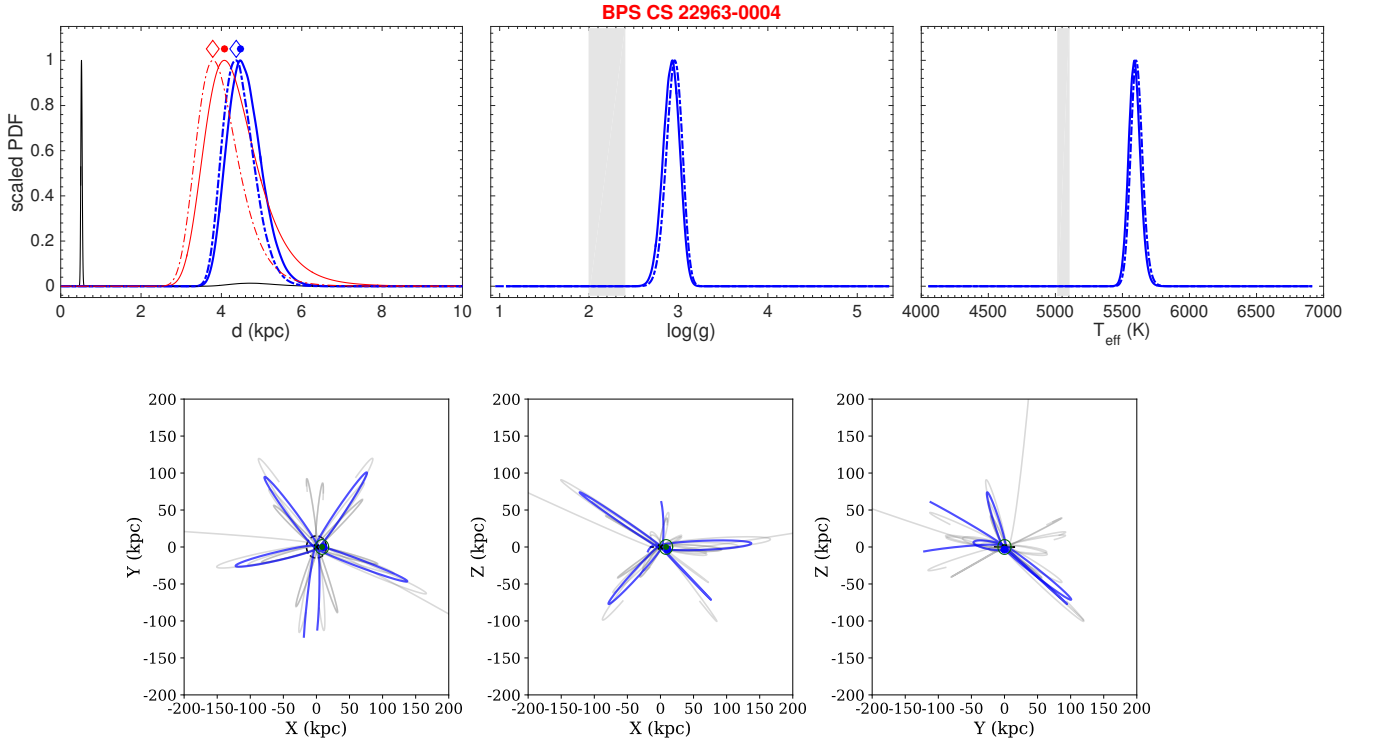


Figure A10. Same as Figure A2, but for BPS CS 22963-0004.

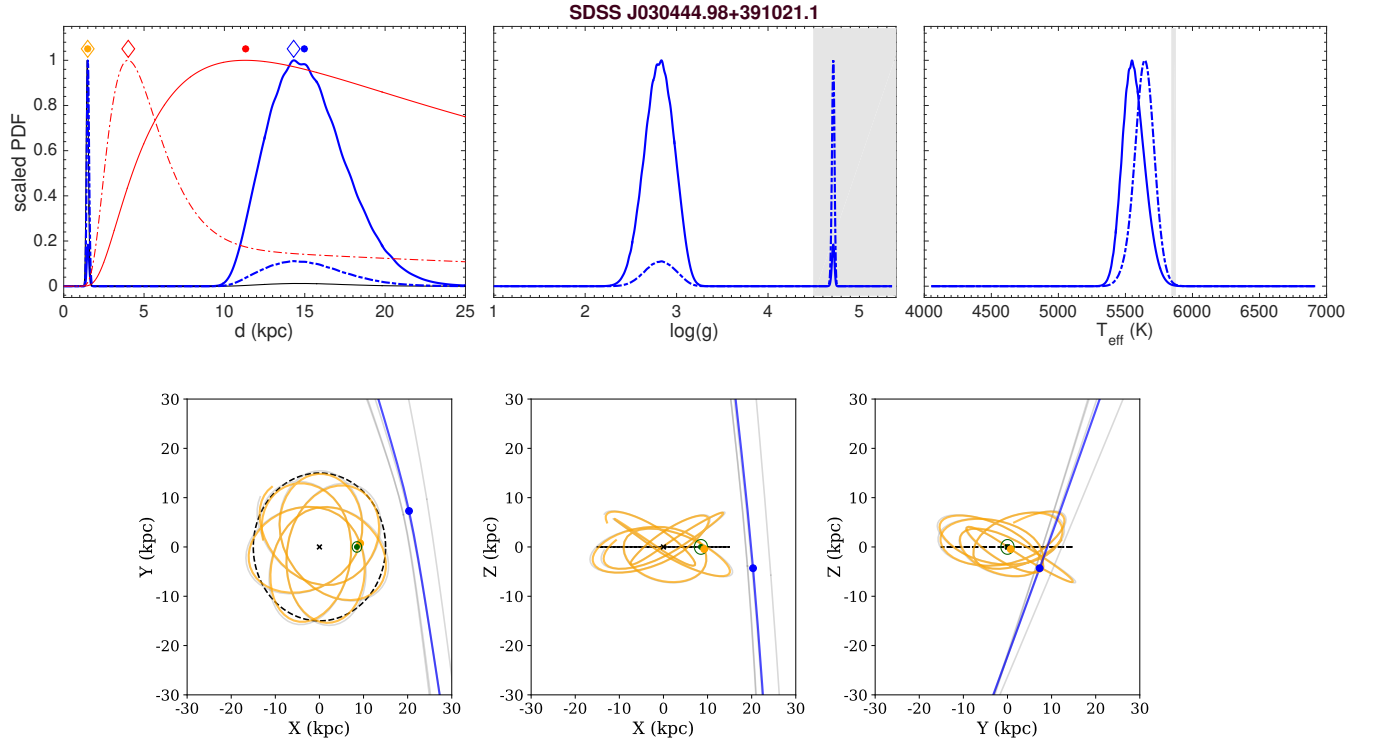


Figure A11. Same as Figure A2, but for SDSS J030444.98+391021.1.

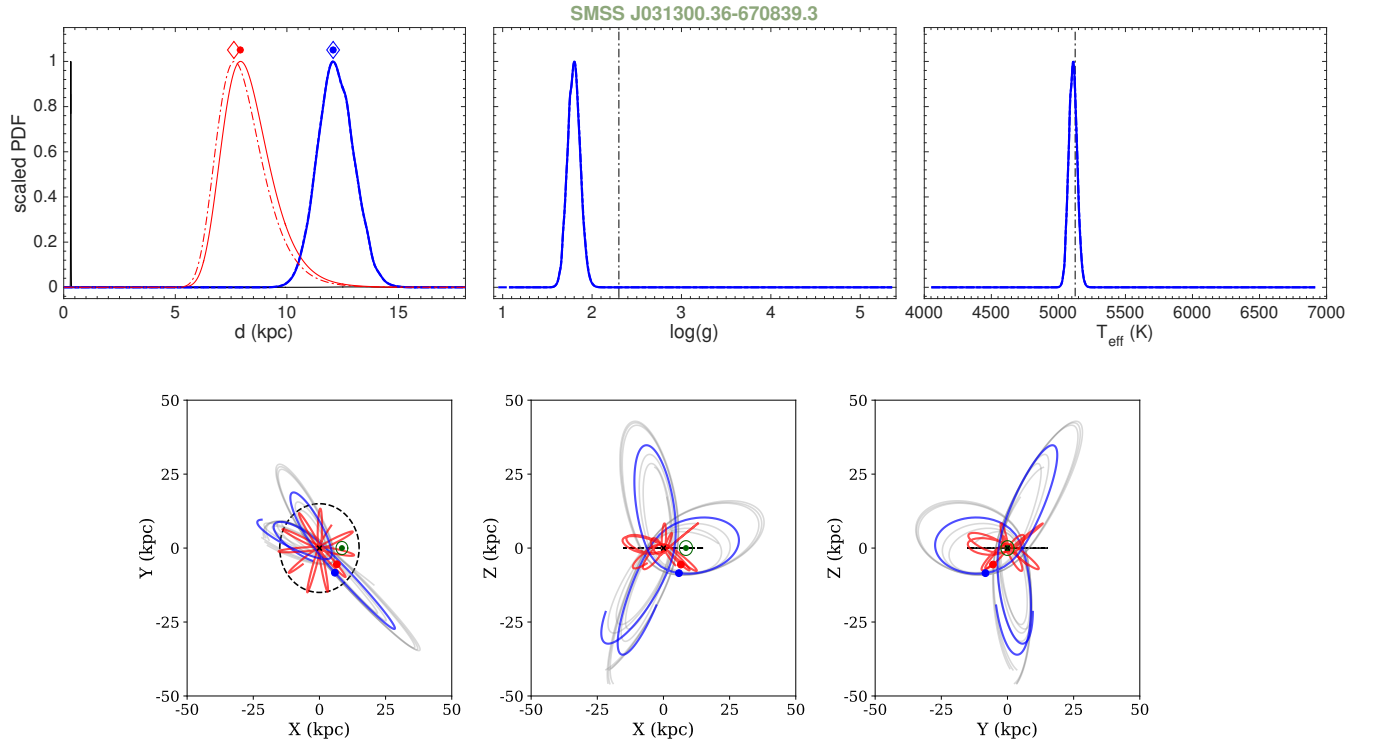


Figure A12. Same as Figure A2, but for SMSS J031300.36-670839.3. For this star, the orbit inferred from the product between the astrometric likelihood and MW halo prior is shown with the red line.

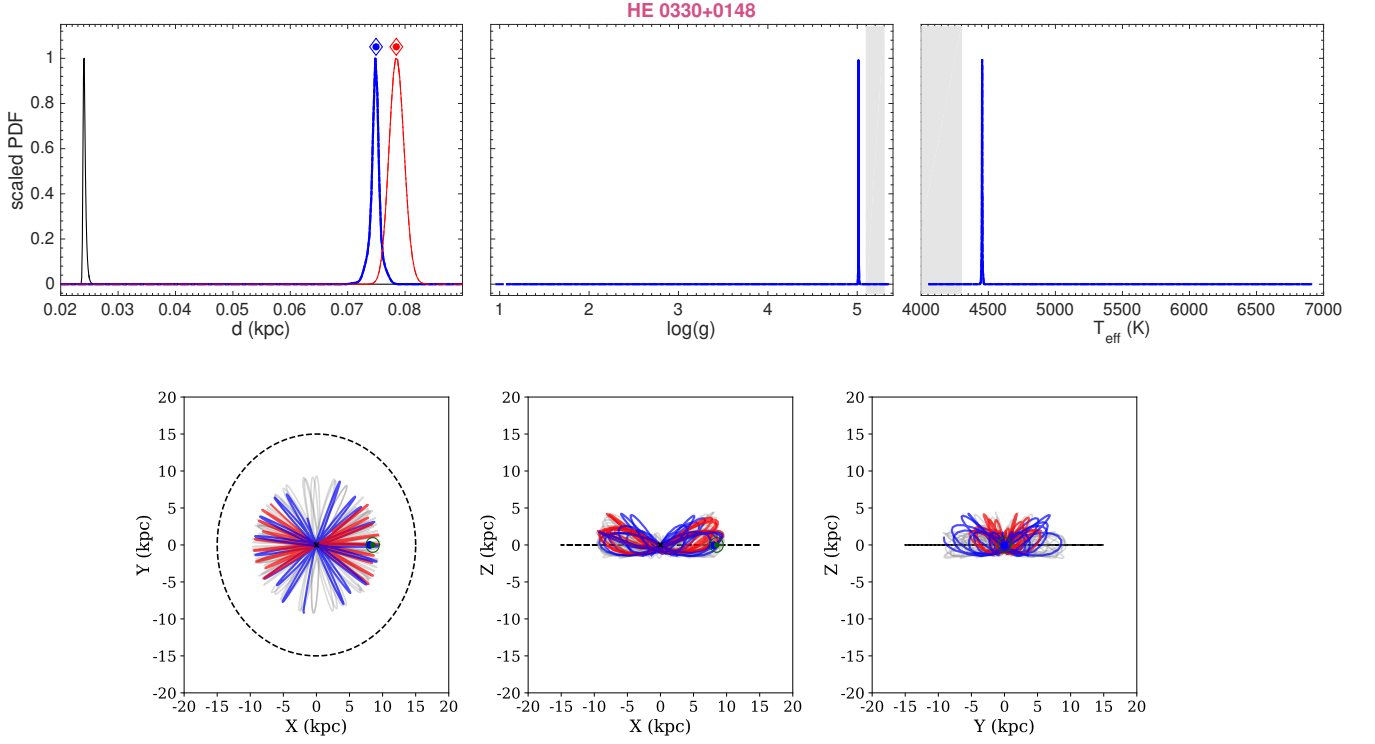


Figure A13. Same as Figure A2, but for HE 0330+0148. For this star, the orbit inferred from the product between the astrometric likelihood and MW halo prior is shown with the red line.

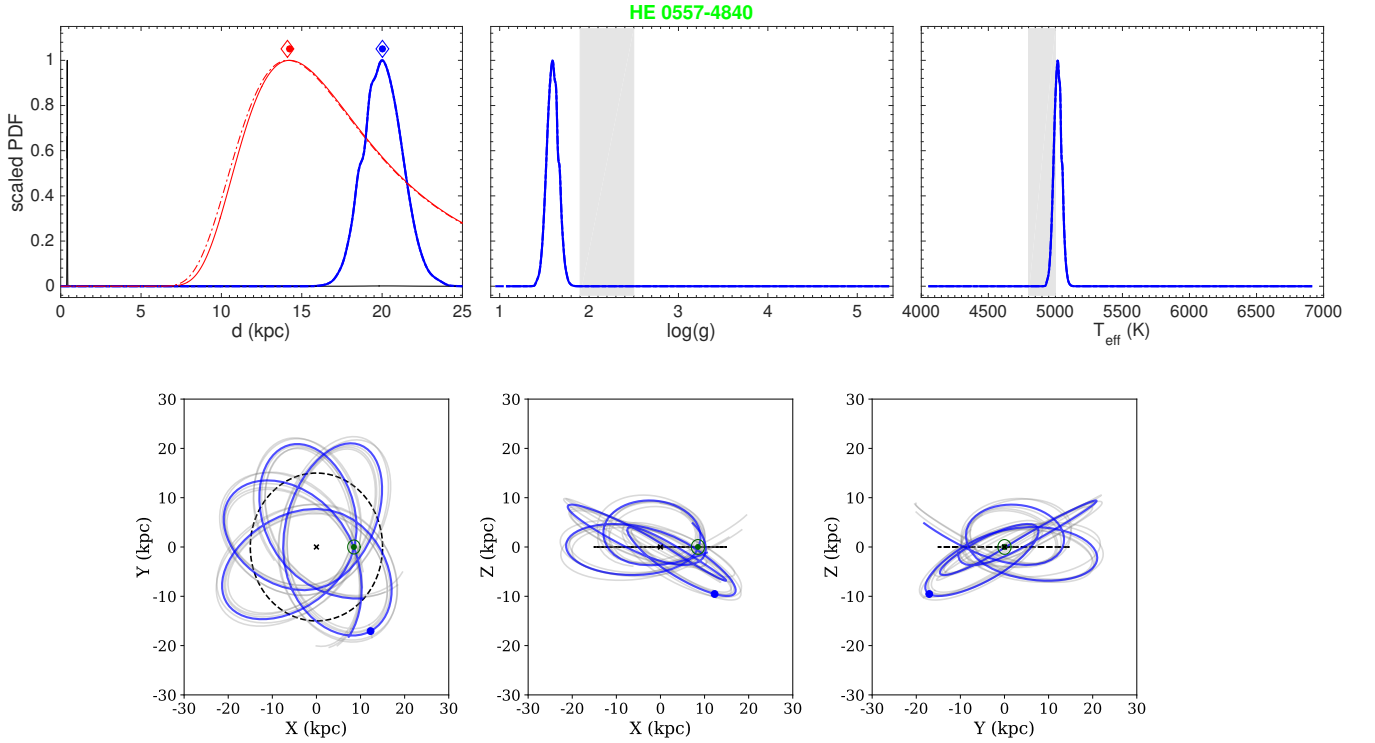


Figure A14. Same as Figure A2, but for HE 0557-4840.

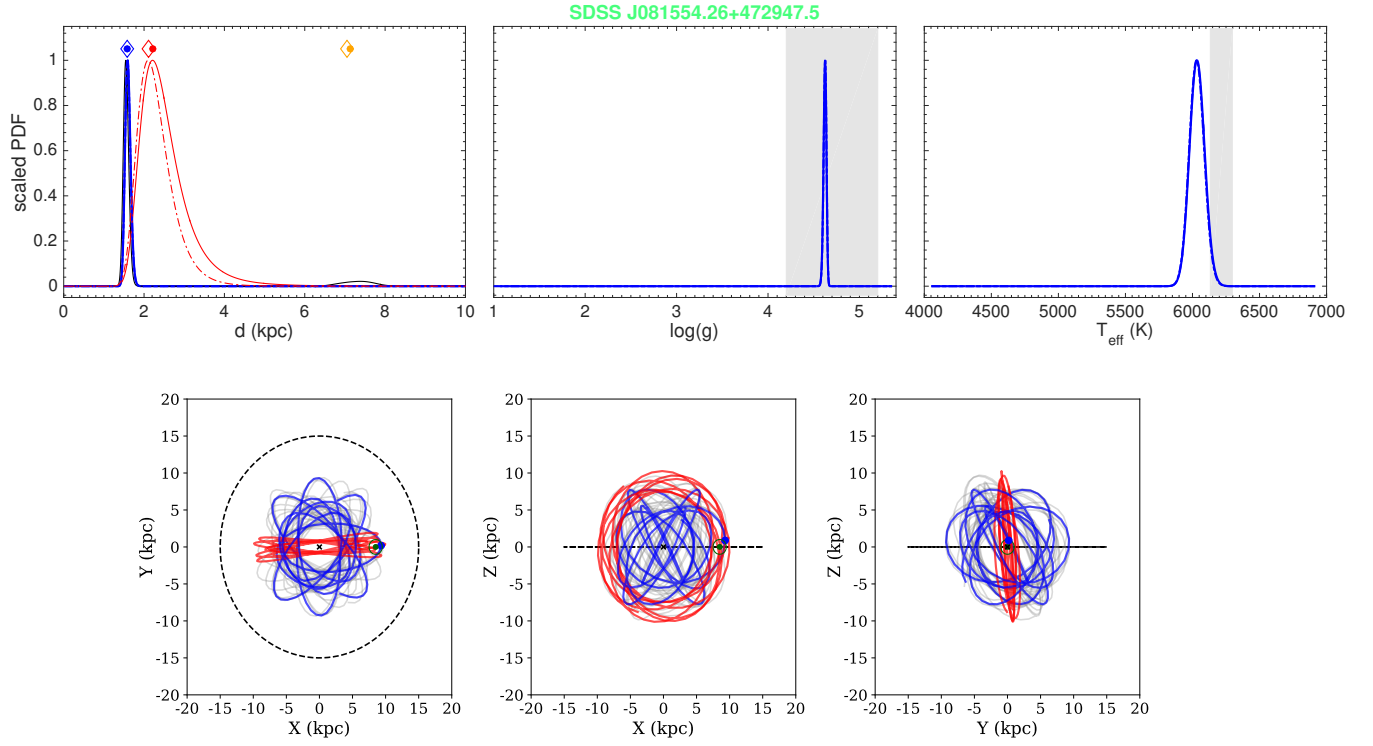


Figure A15. Same as Figure A2, but for SDSS J081554.26+472947.5. For this star, the orbit inferred from the product between the astrometric likelihood and MW halo prior is shown with the red line.

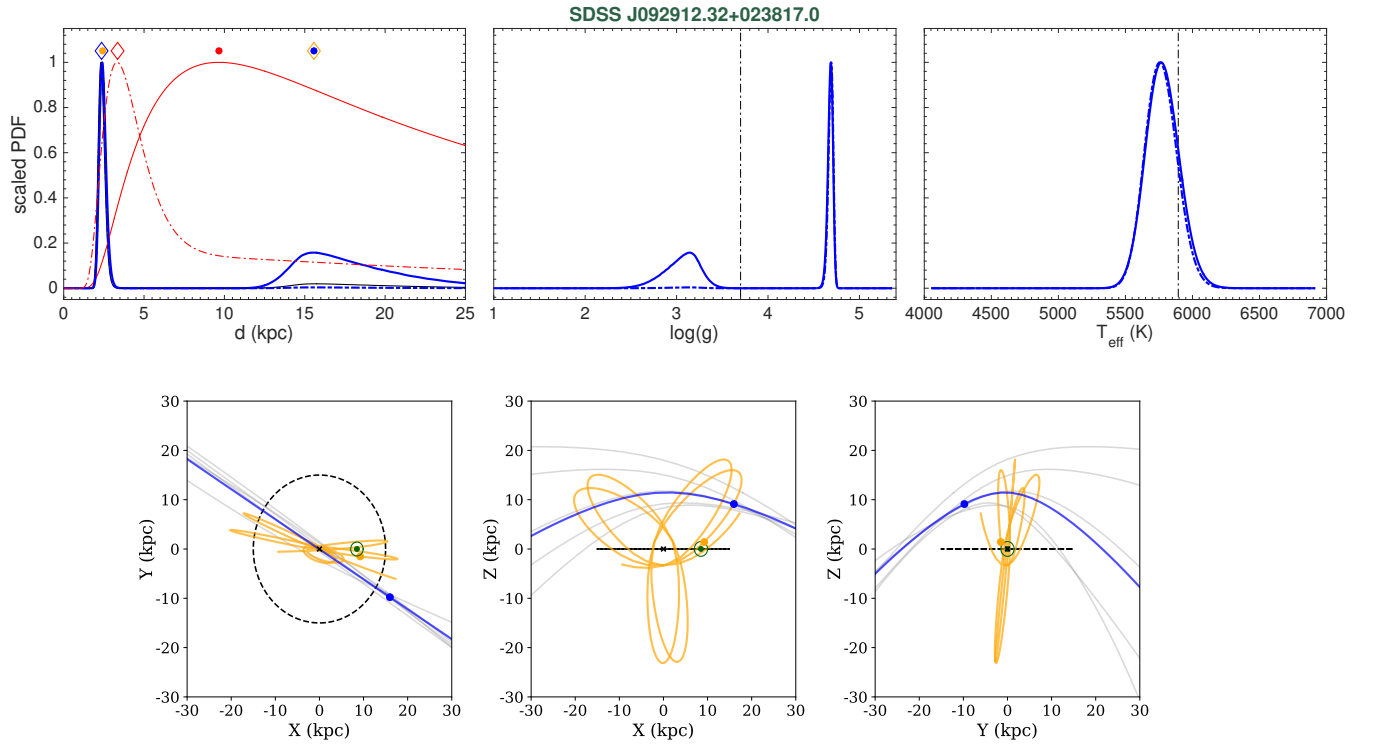


Figure A16. Same as Figure A2, but for SDSS J092912.32+023817.0.

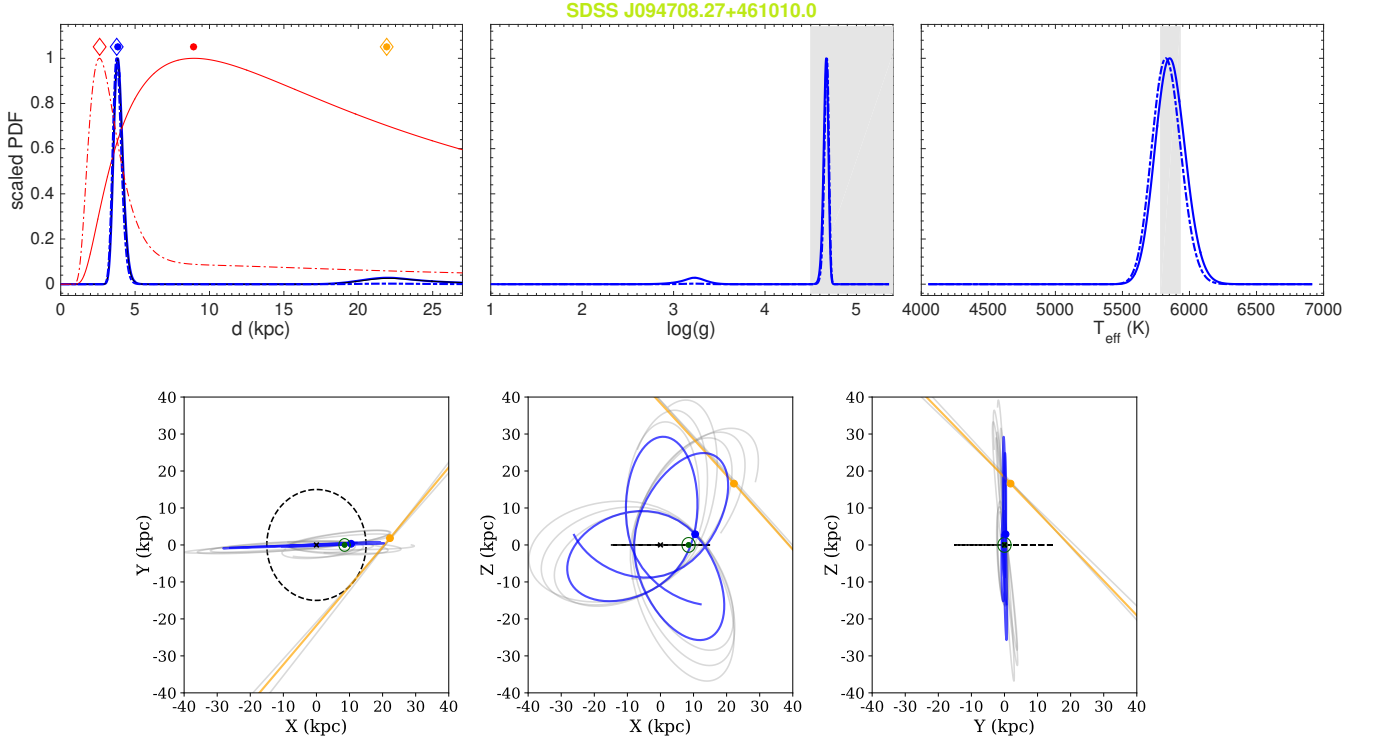


Figure A17. Same as Figure A2, but for SDSS J094708.27+461010.0.

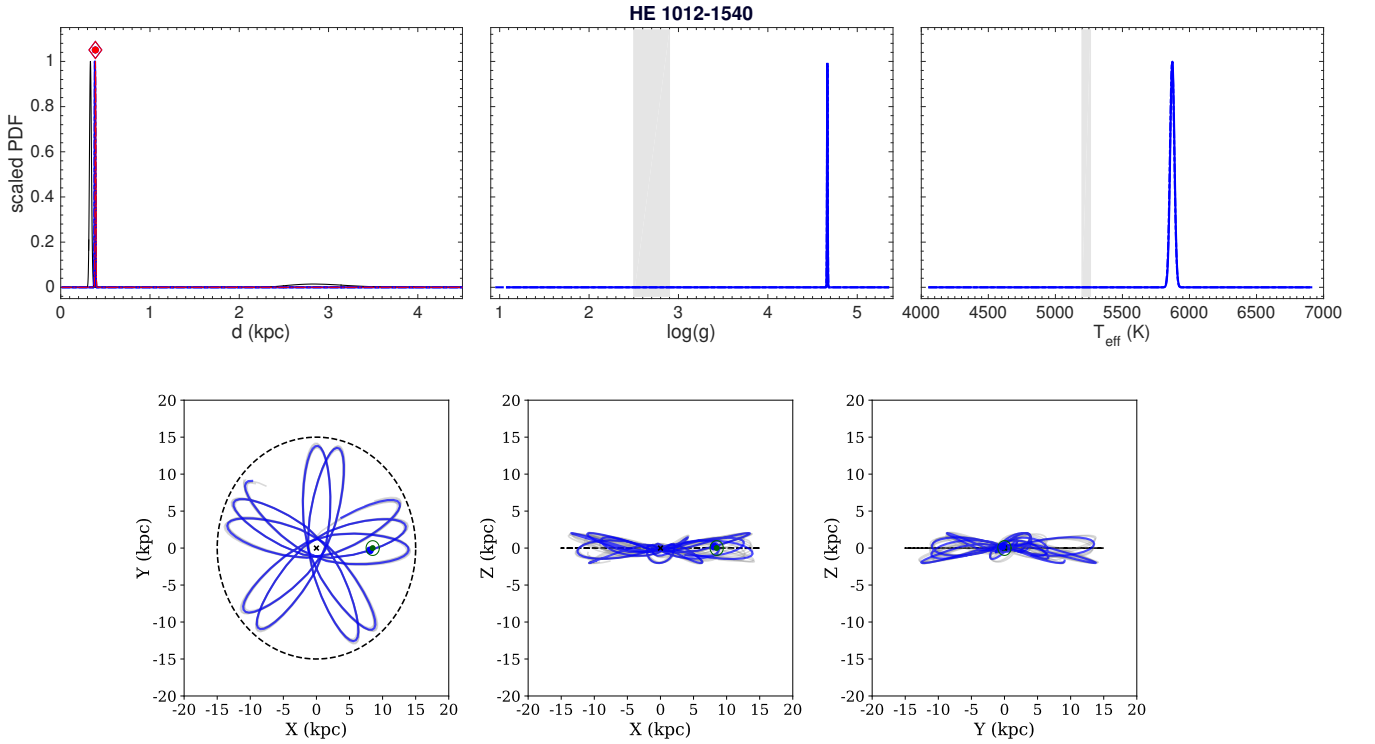


Figure A18. Same as Figure A2, but for HE 1012-1540.

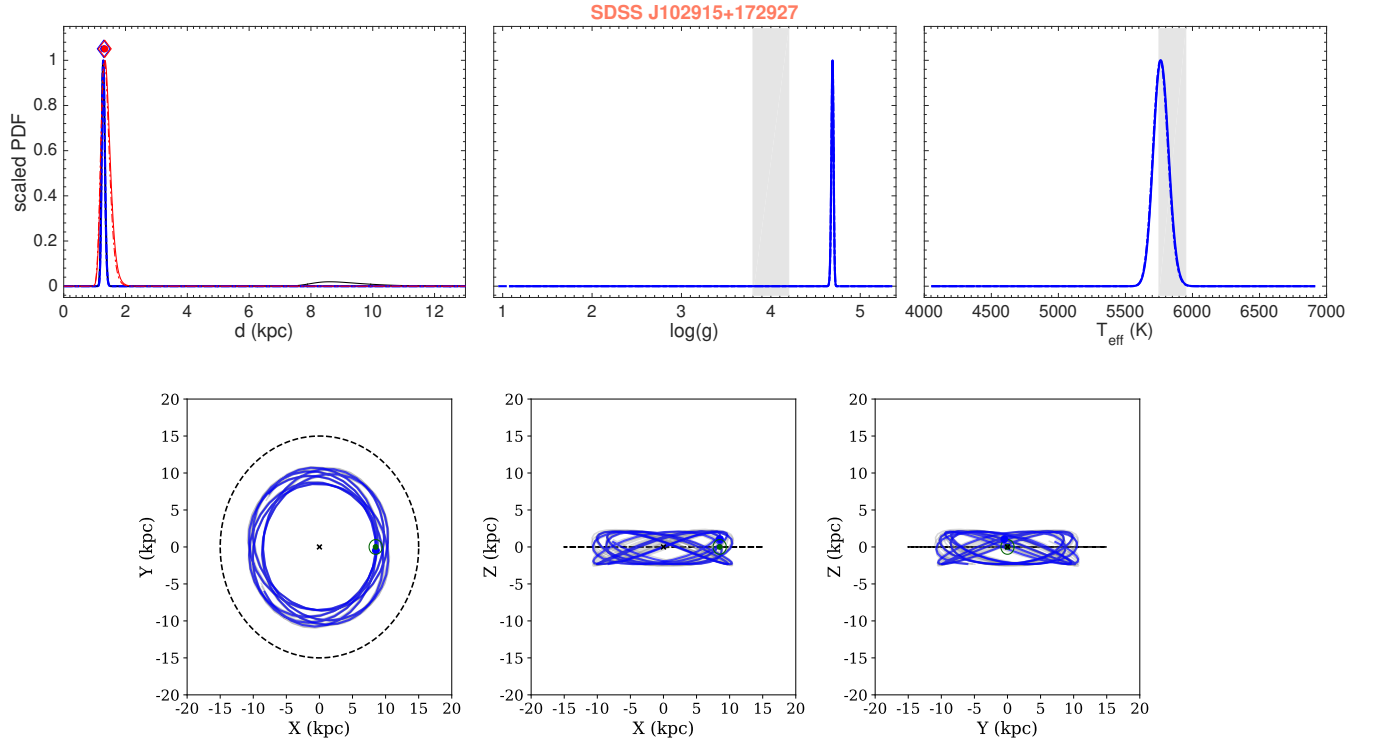


Figure A19. Same as Figure A2, but for SDSS J102915+172927.

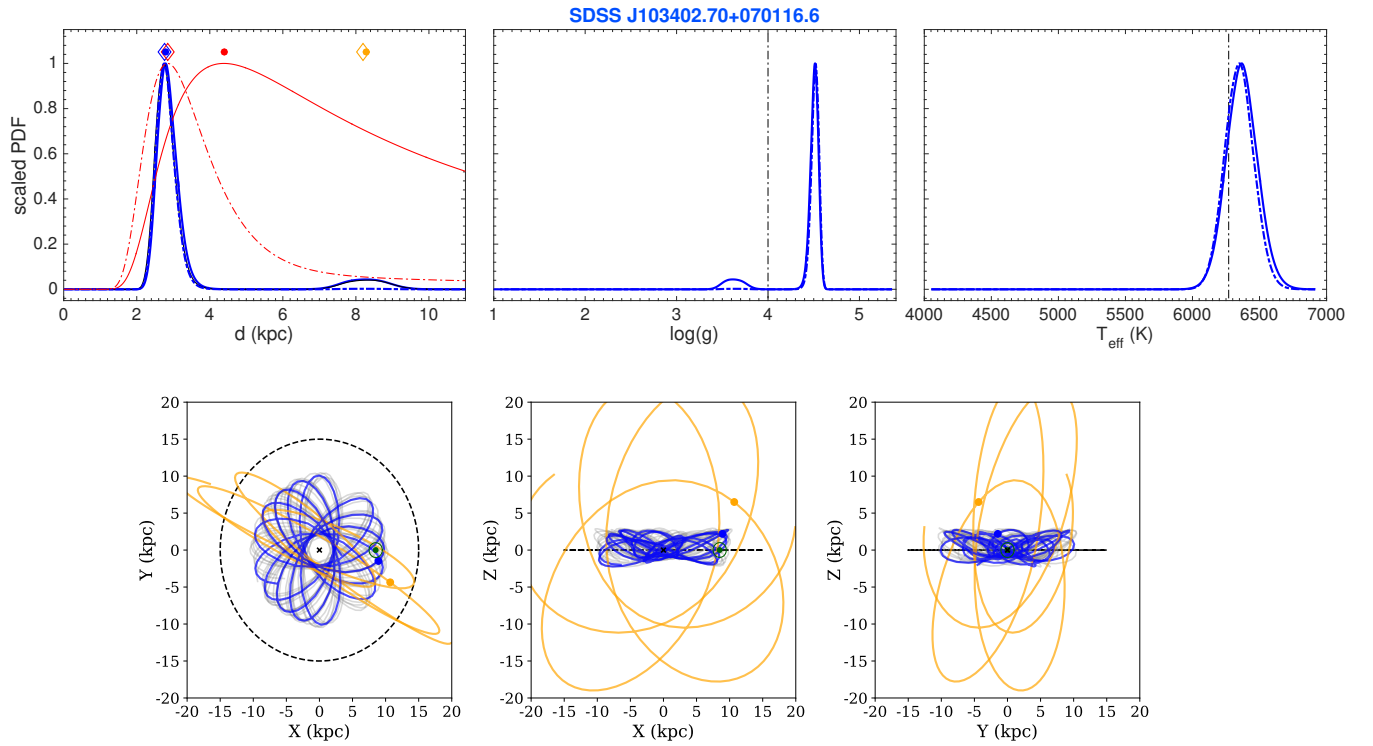


Figure A20. Same as Figure A2, but for SDSS J103402.70+070116.6.

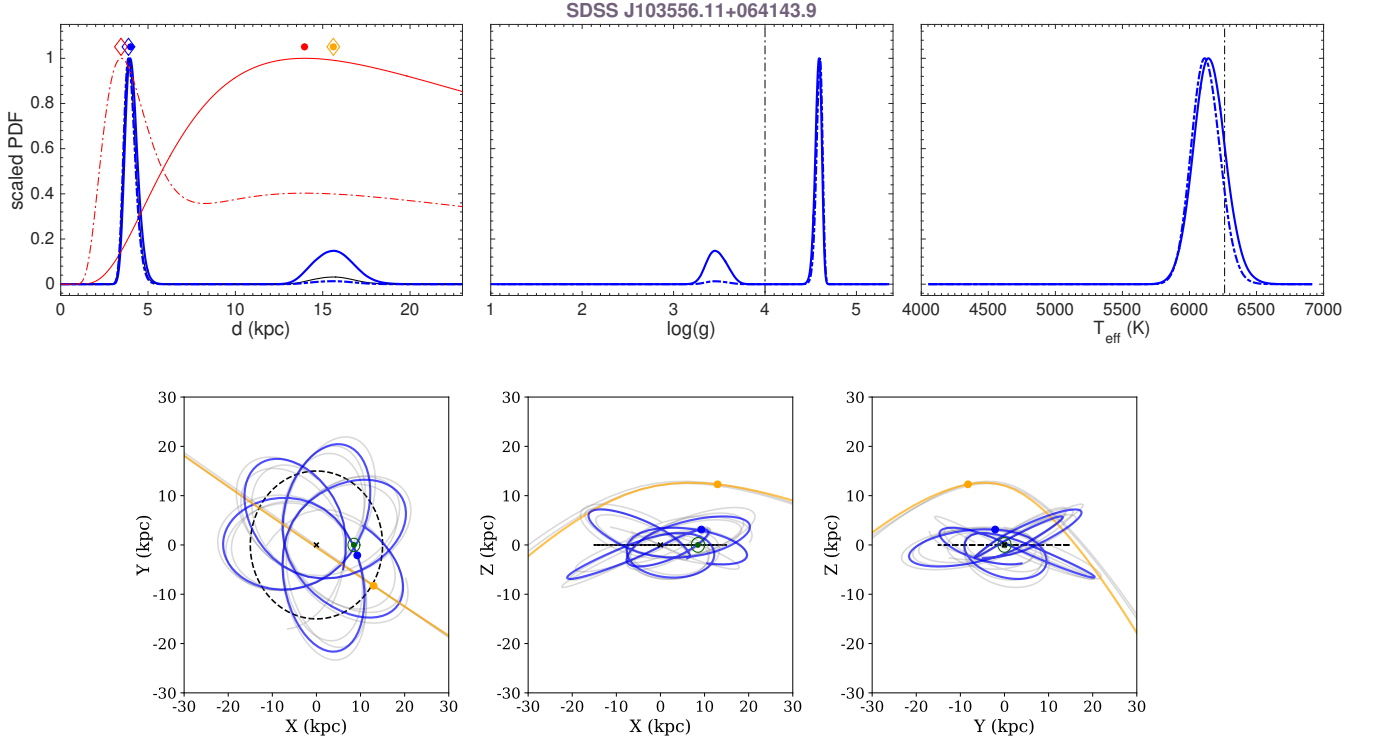


Figure A21. Same as Figure A2, but for SDSS J103556.11+064143.9.

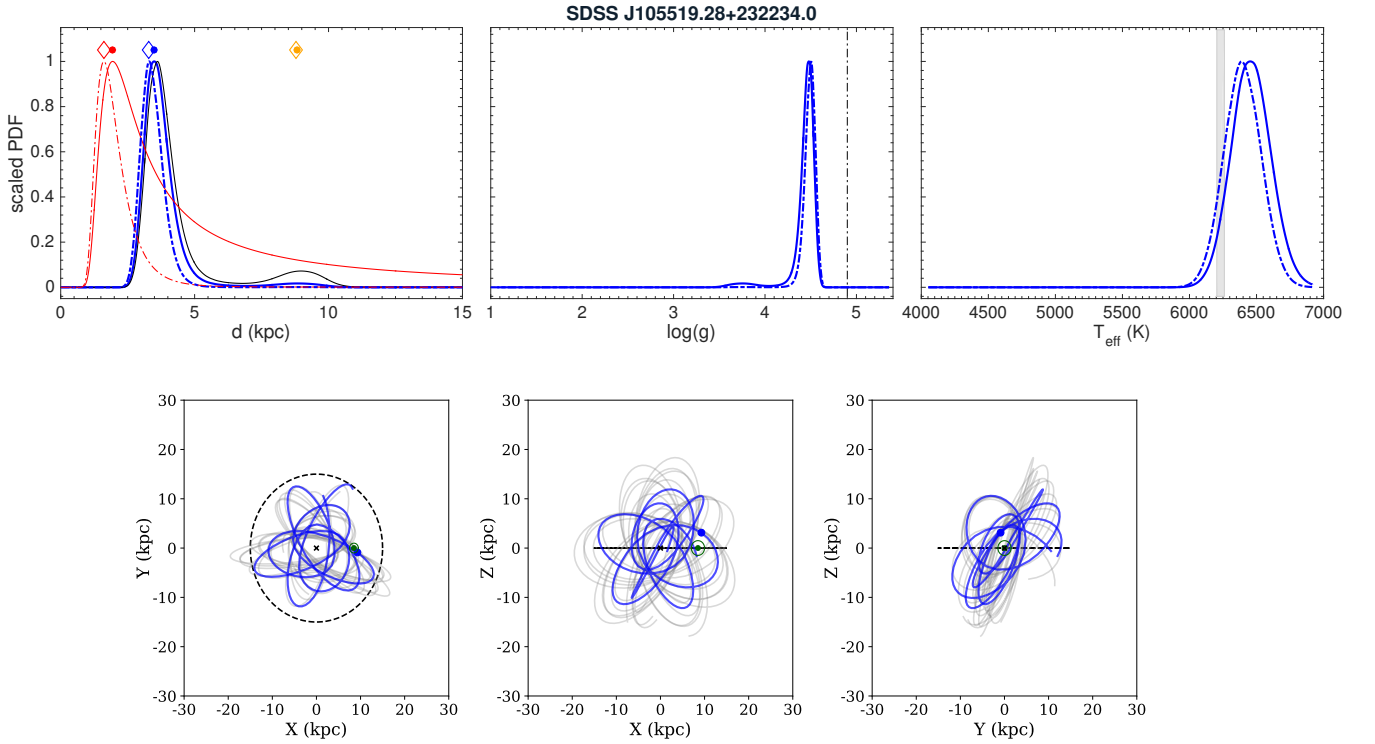


Figure A22. Same as Figure A2, but for SDSS J105519.28+232234.0.

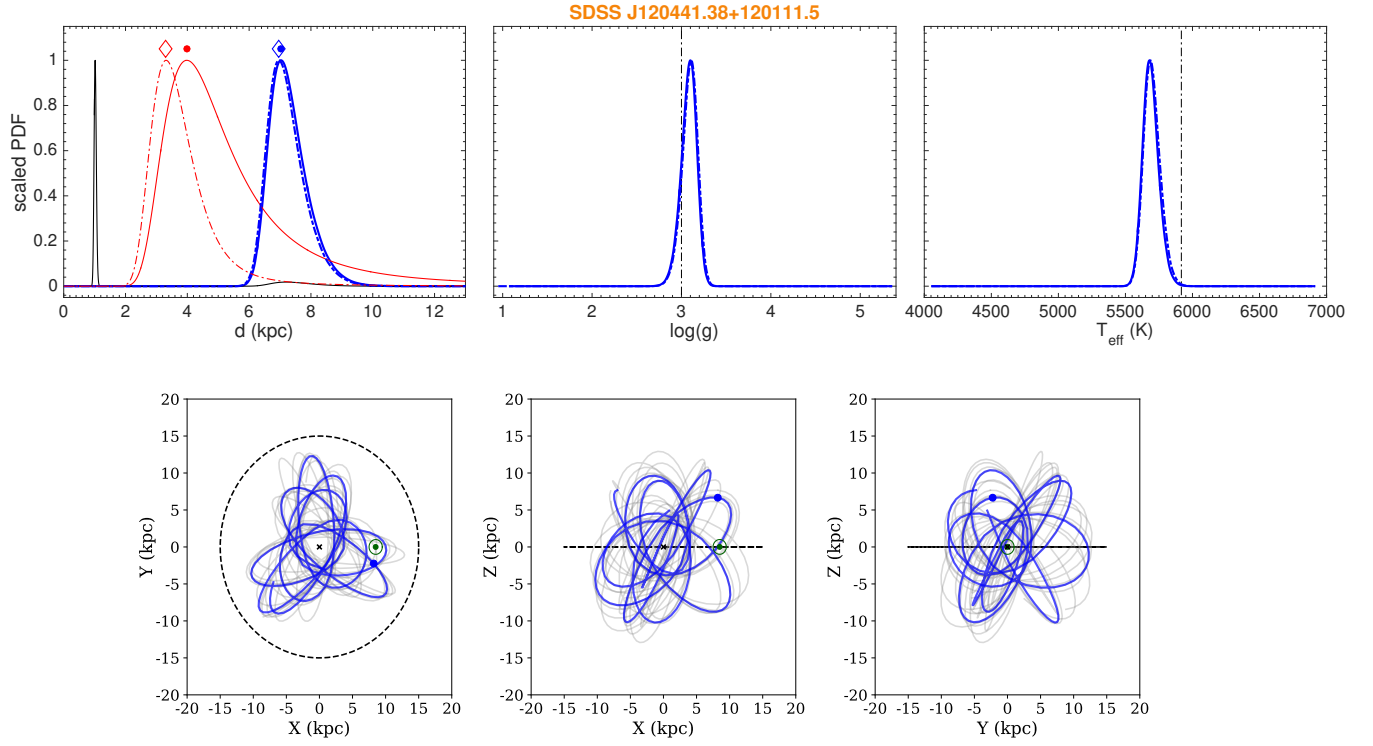


Figure A23. Same as Figure A2, but for SDSS J120441.38+120111.5.

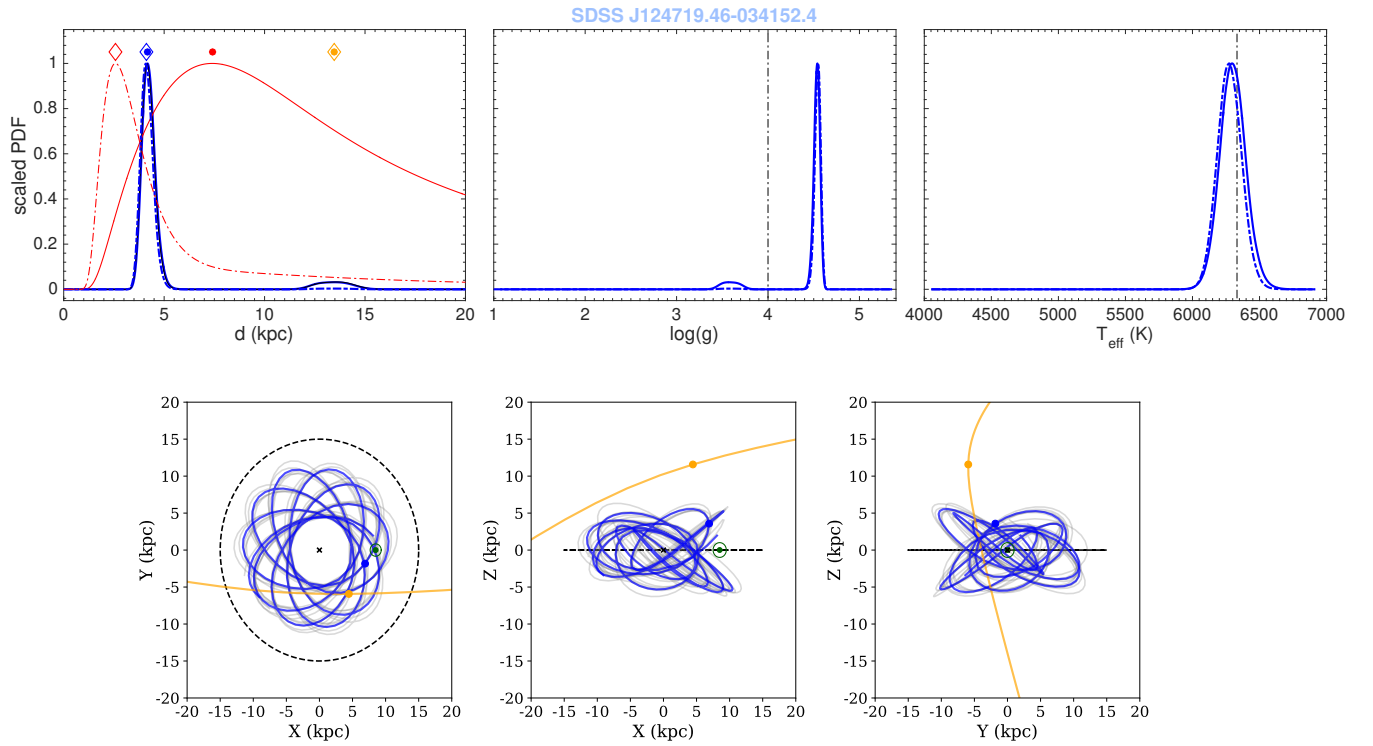


Figure A24. Same as Figure A2, but for SDSS J124719.46-034152.4.

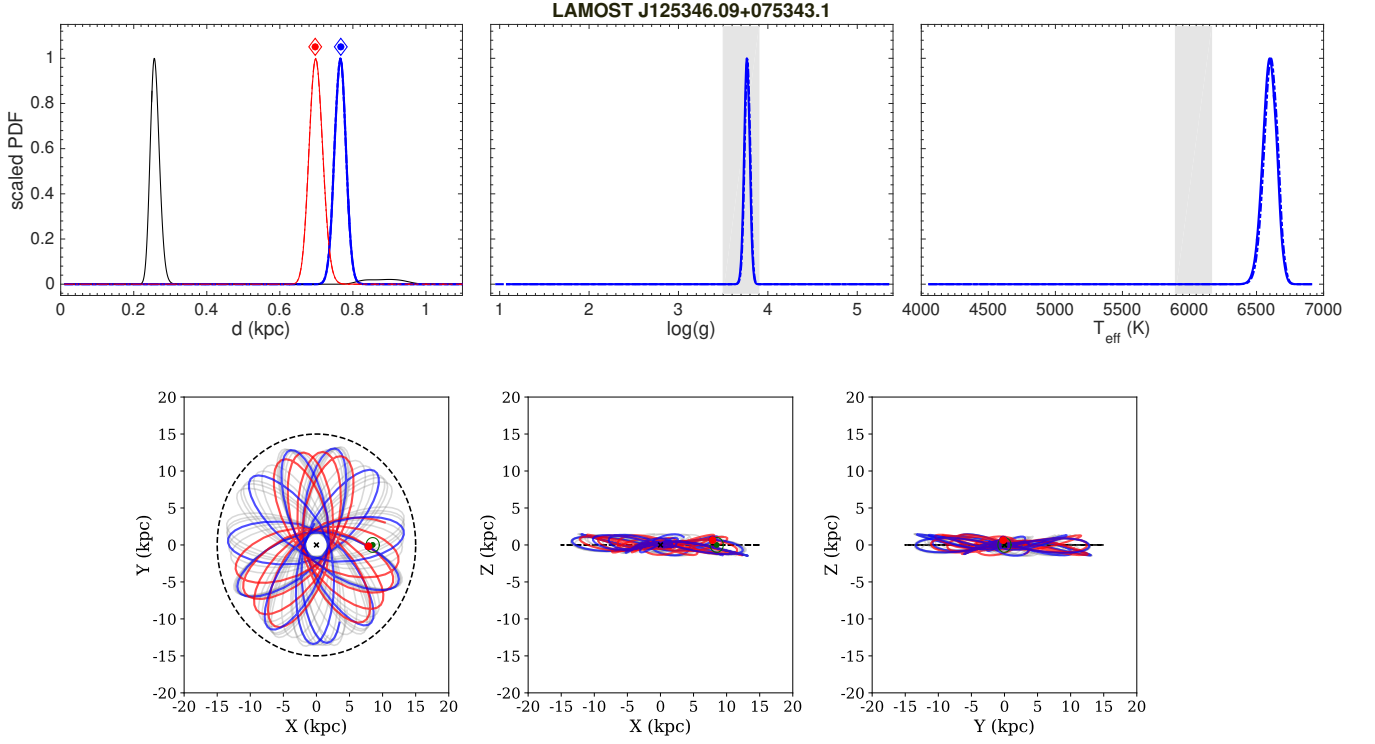


Figure A25. Same as Figure A2, but for LAMOST J125346.09+075343.1. For this star, the orbit inferred from the product between the astrometric likelihood and MW halo prior is shown with the red line.

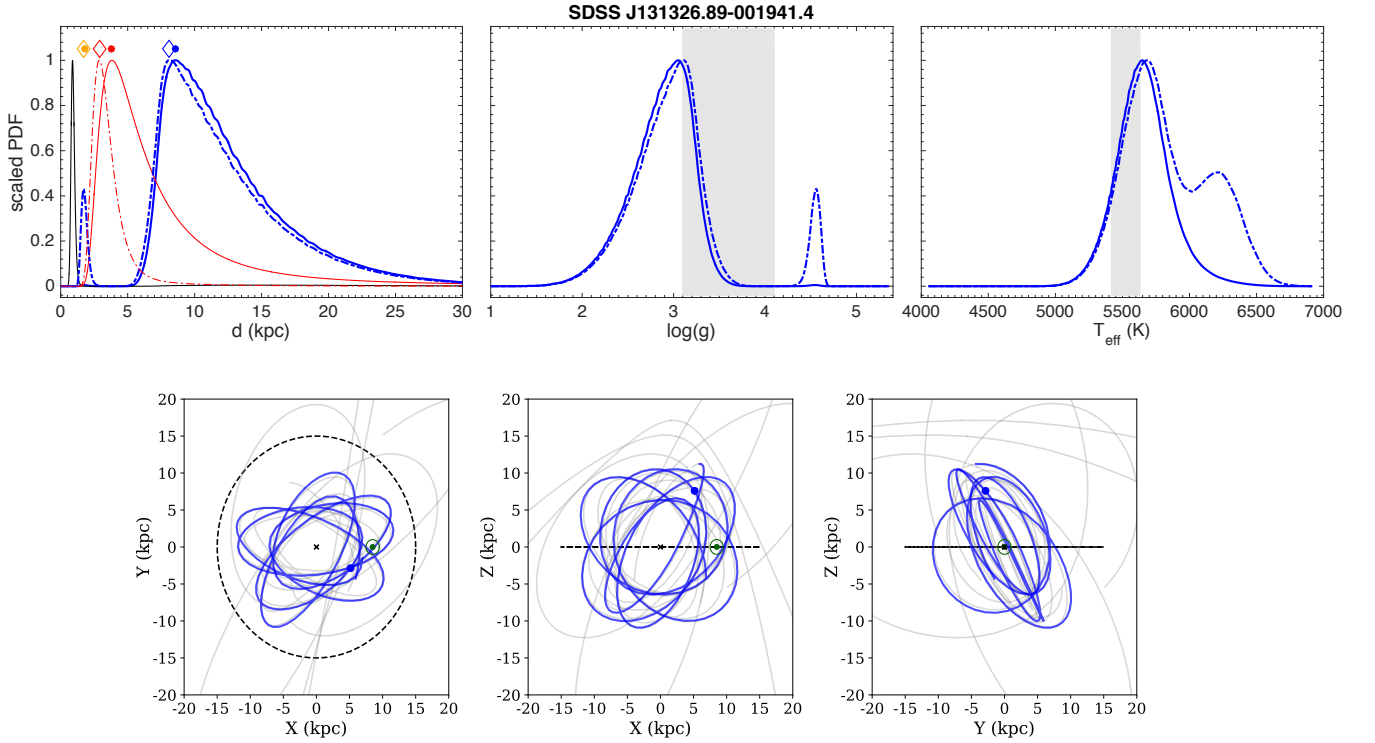


Figure A26. Same as Figure A2, but for SDSS J131326.89-001941.4.

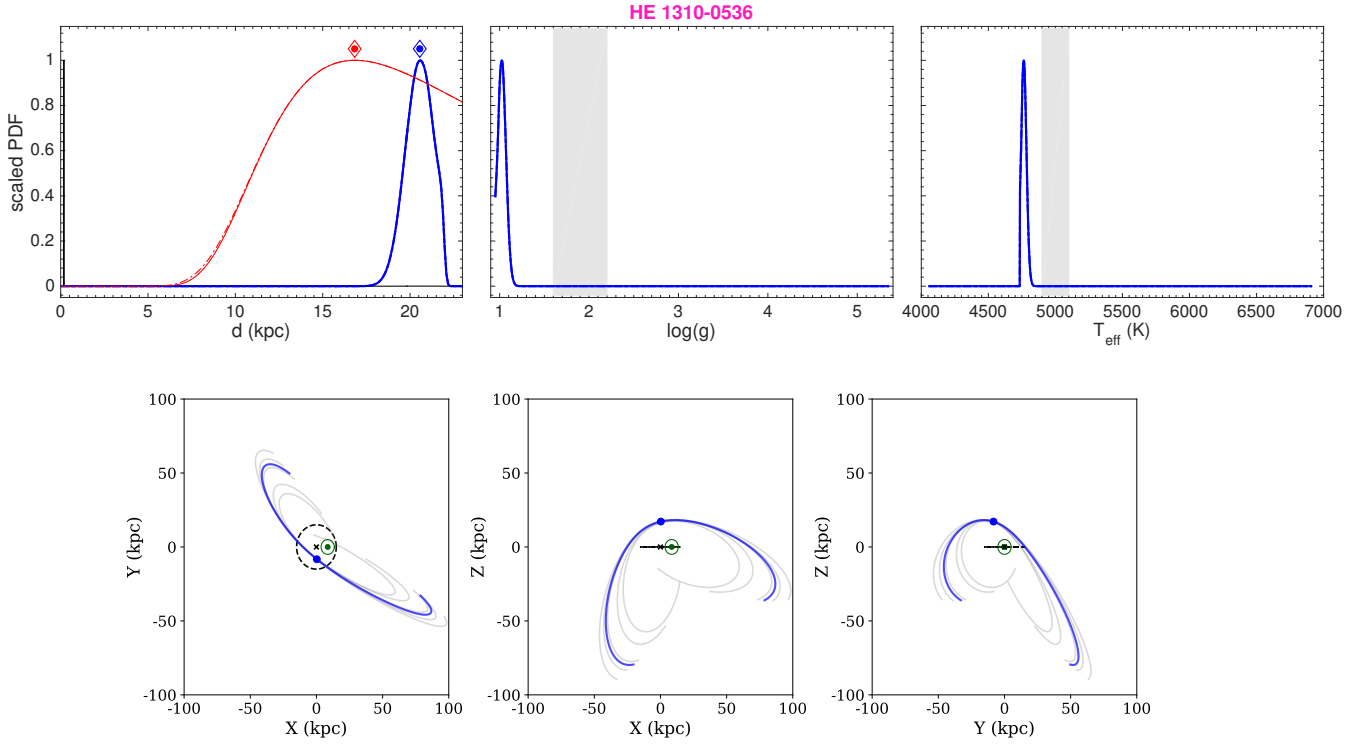


Figure A27. Same as Figure A2, but for HE 1310-0536.

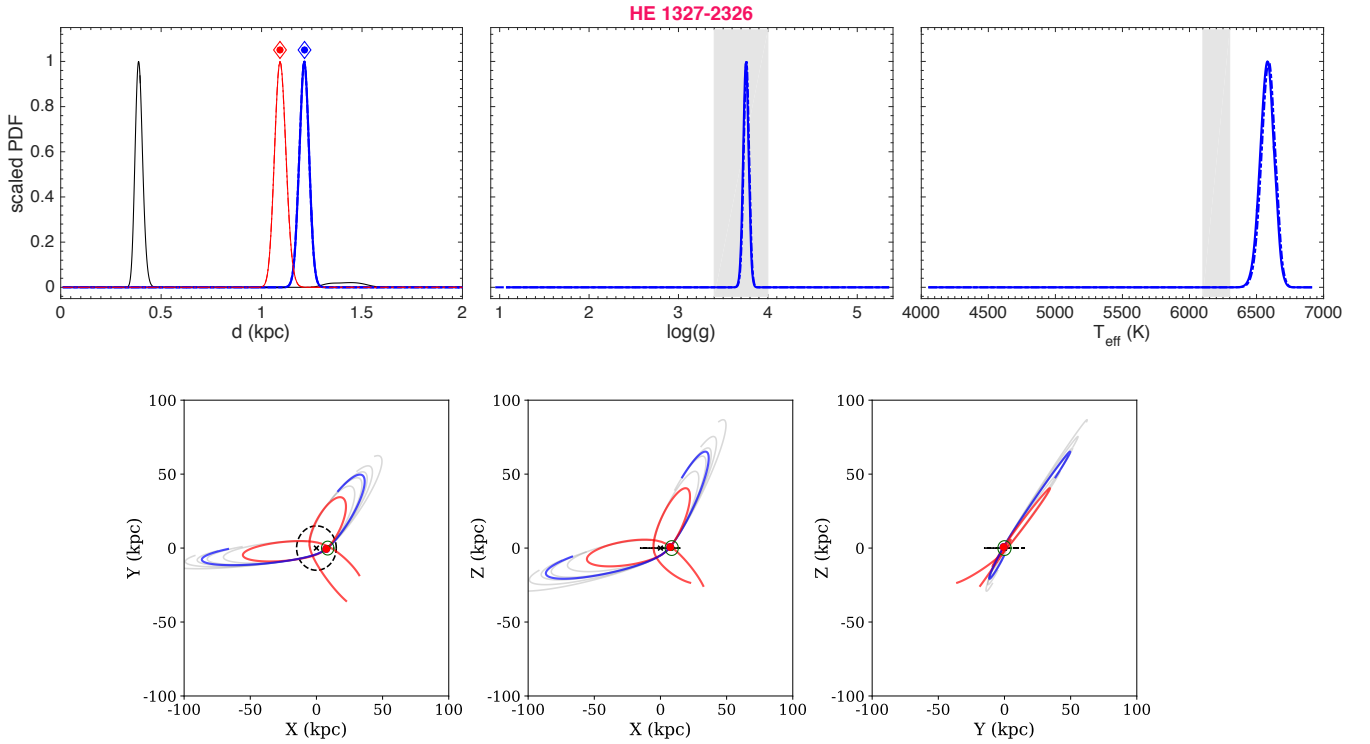


Figure A28. Same as Figure A2, but for HE 1327-2326. For this star, the orbit inferred from the product between the astrometric likelihood and MW halo prior is shown with the red line.

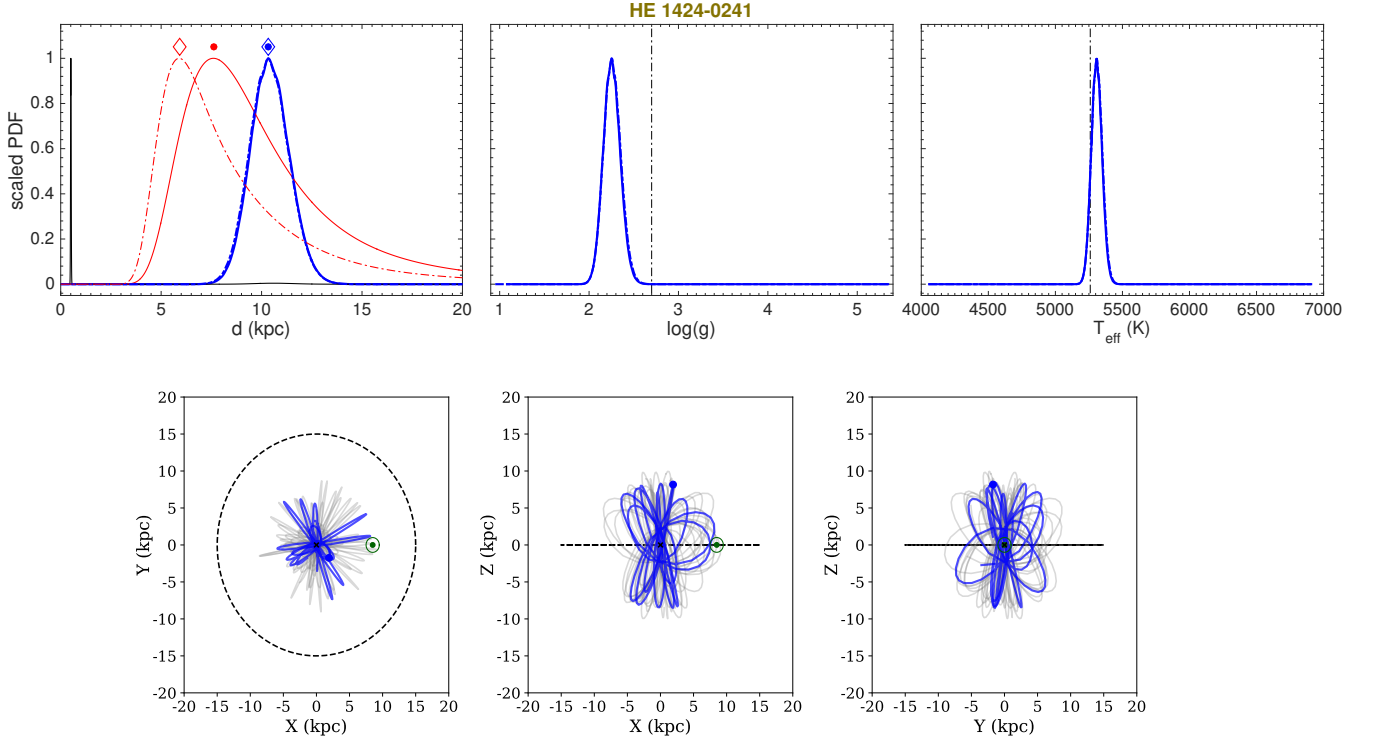


Figure A29. Same as Figure A2, but for HE 1424-0241.

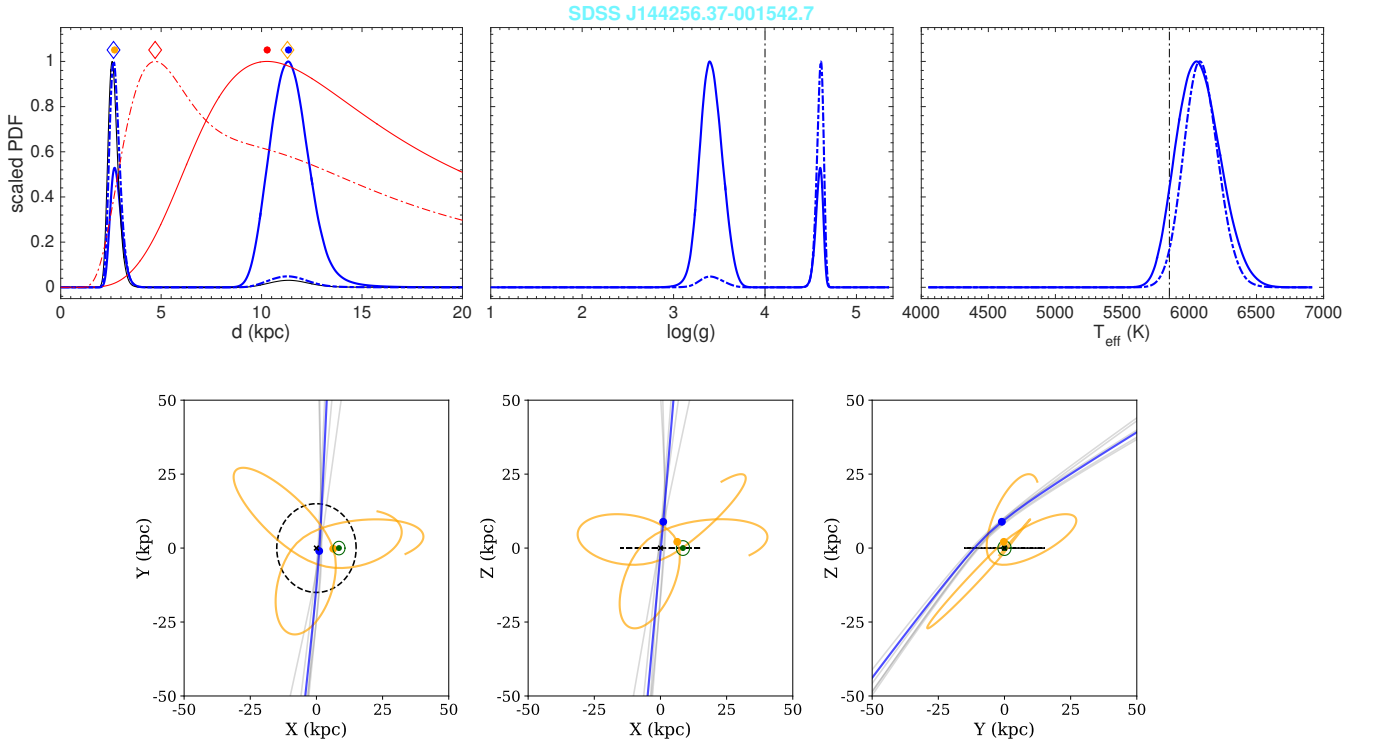


Figure A30. Same as Figure A2, but for SDSS J144256.37-001542.7.

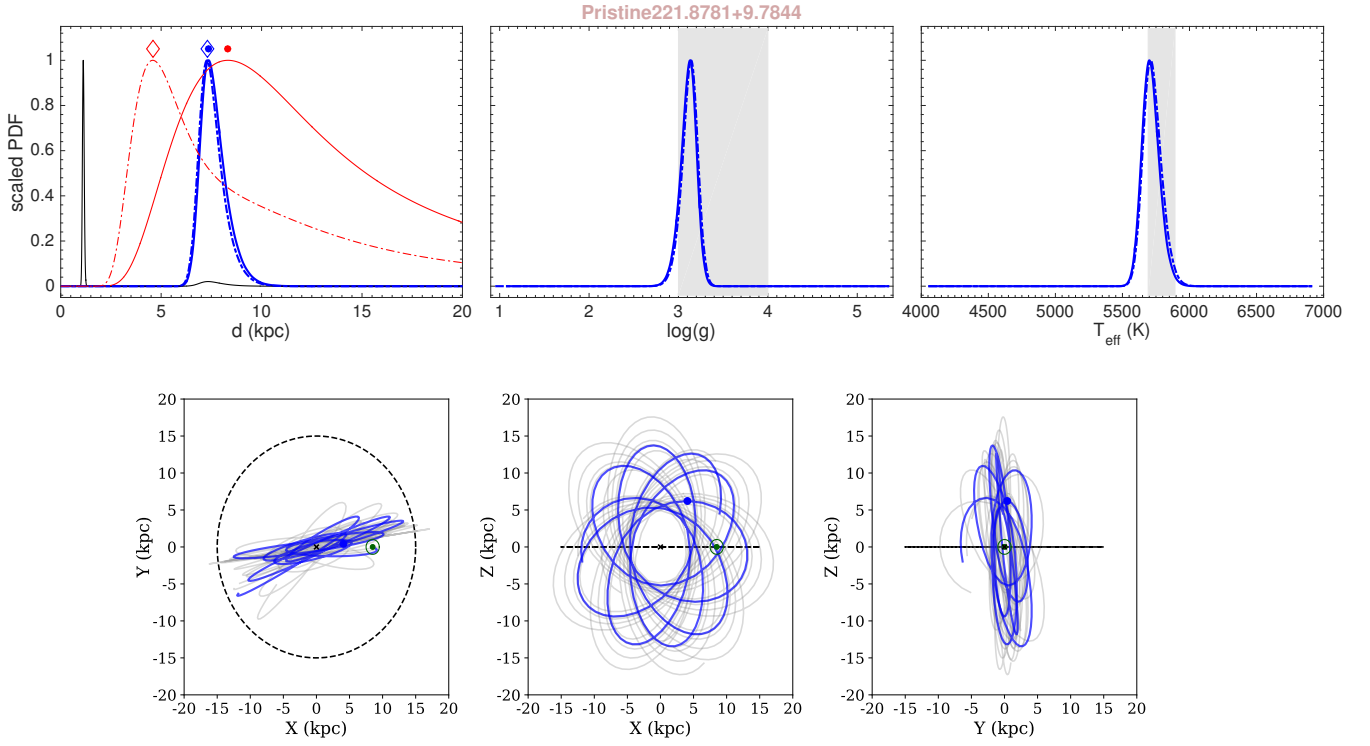


Figure A31. Same as Figure A2, but for Pristine221.8781+9.7844.

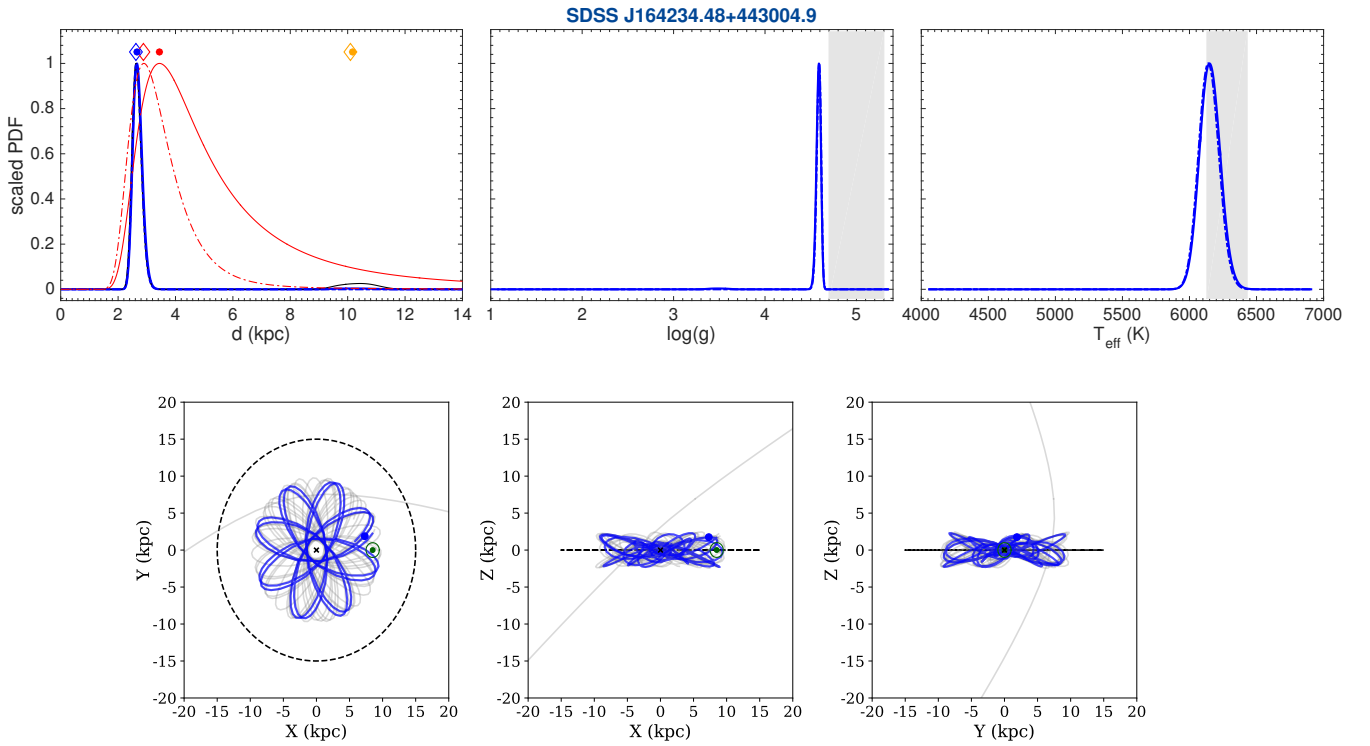


Figure A32. Same as Figure A2, but for SDSS J164234.48+443004.9.

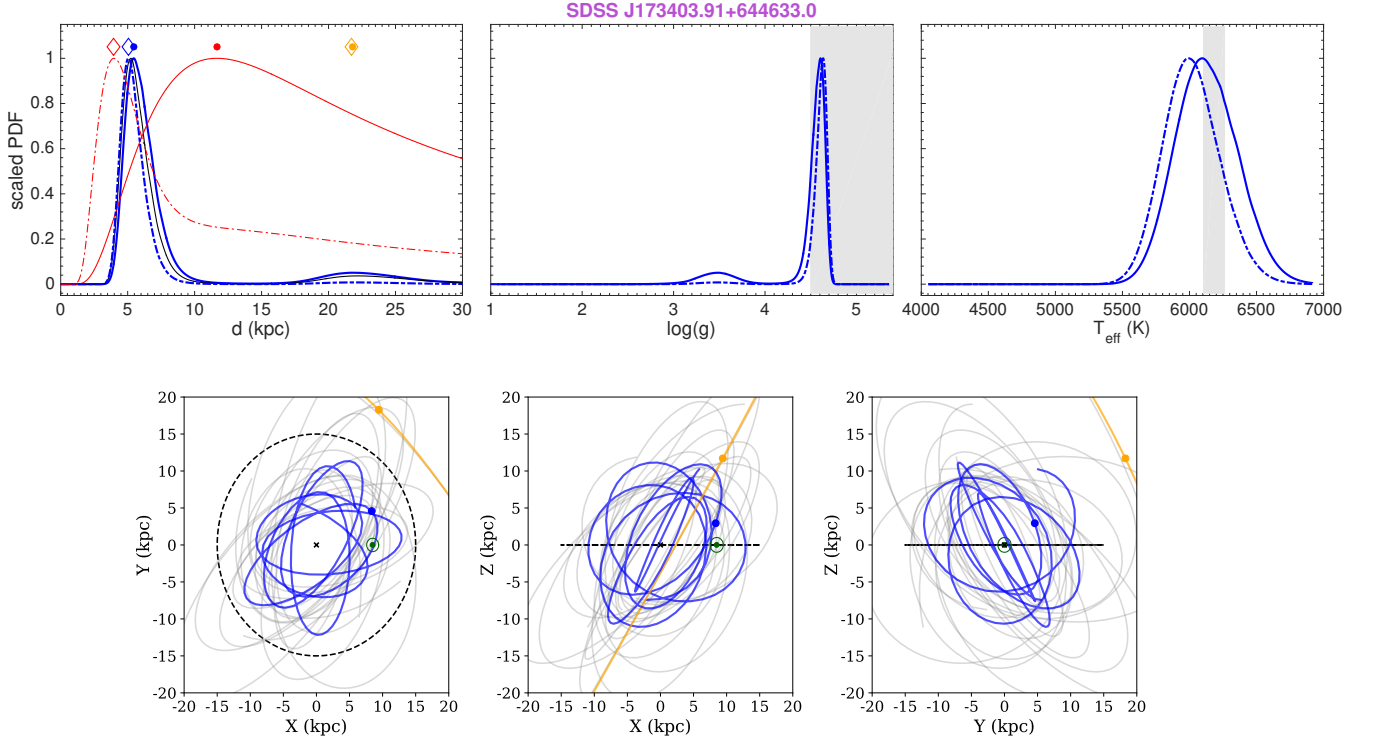


Figure A33. Same as Figure A2, but for SDSS J173403.91+644633.0.

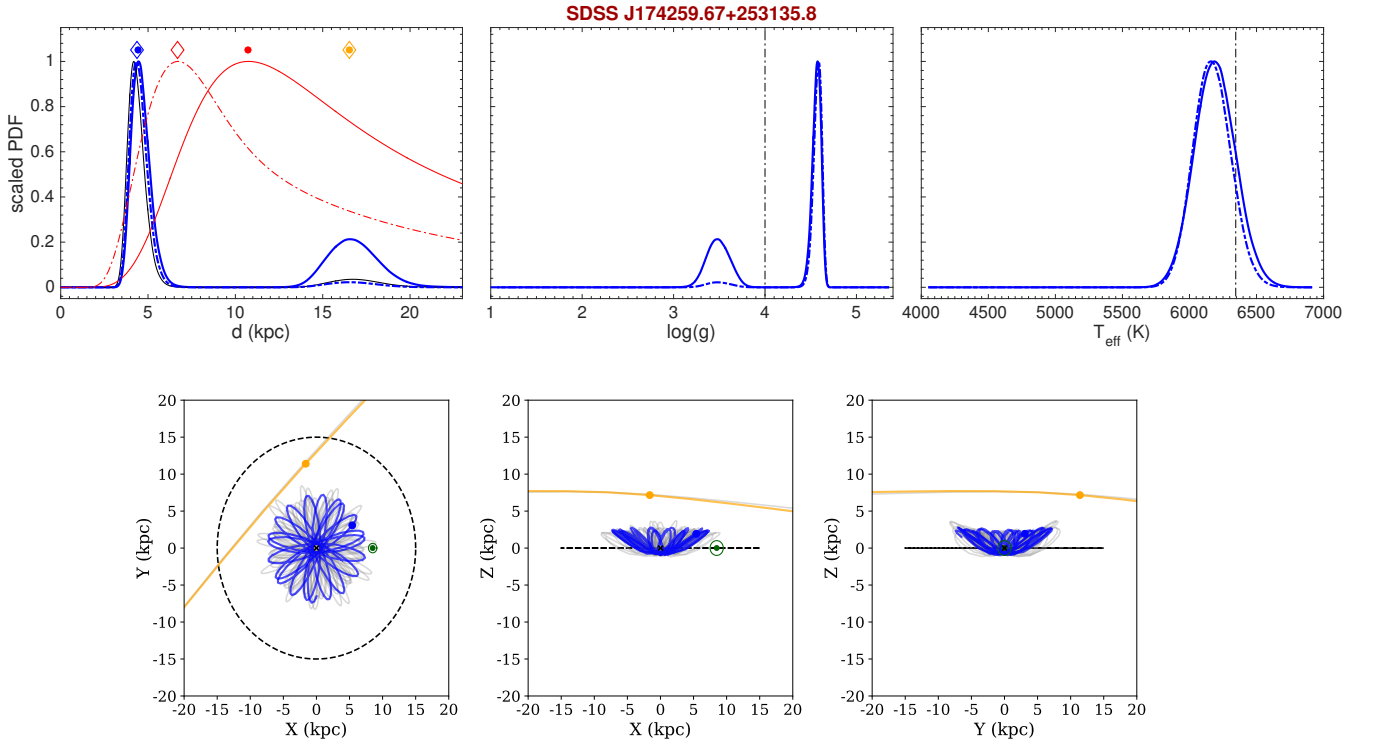


Figure A34. Same as Figure A2, but for SDSS J174259.67+253135.8.

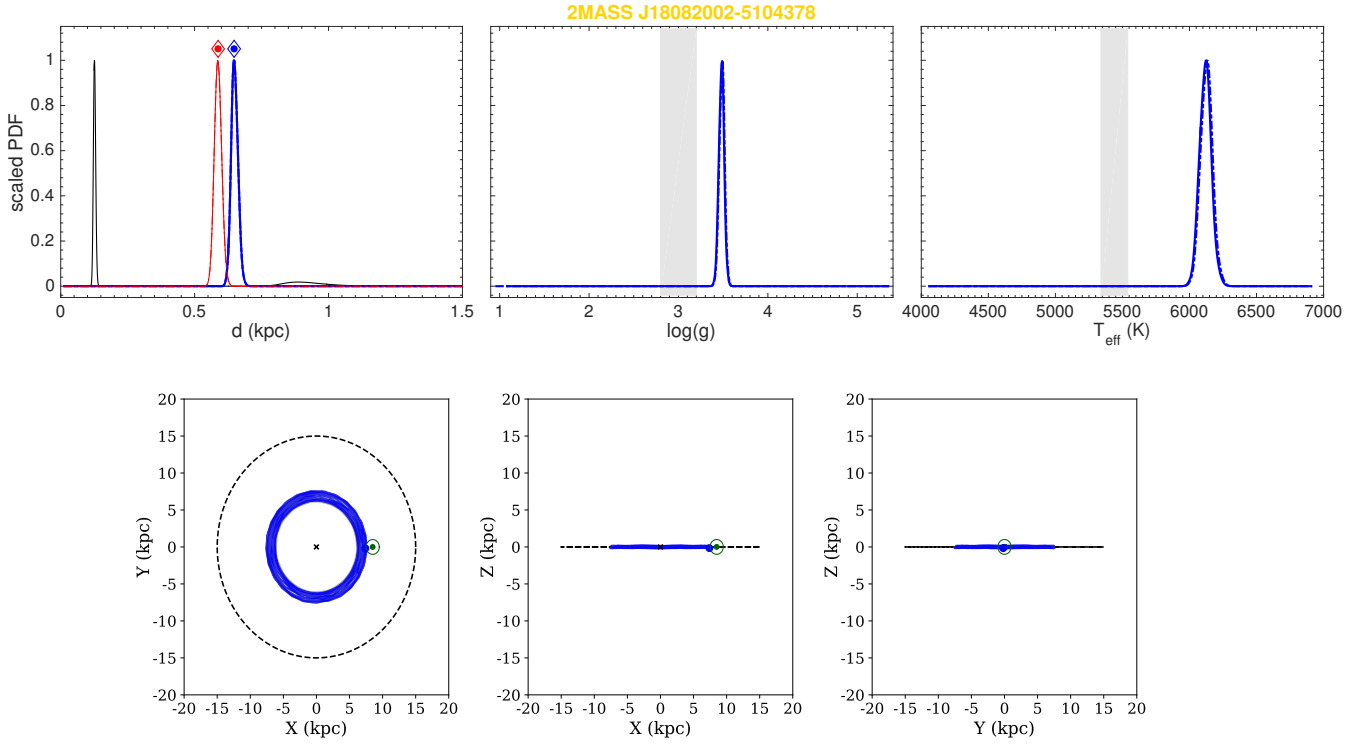


Figure A35. Same as Figure A2, but for 2MASS J18082002-5104378.

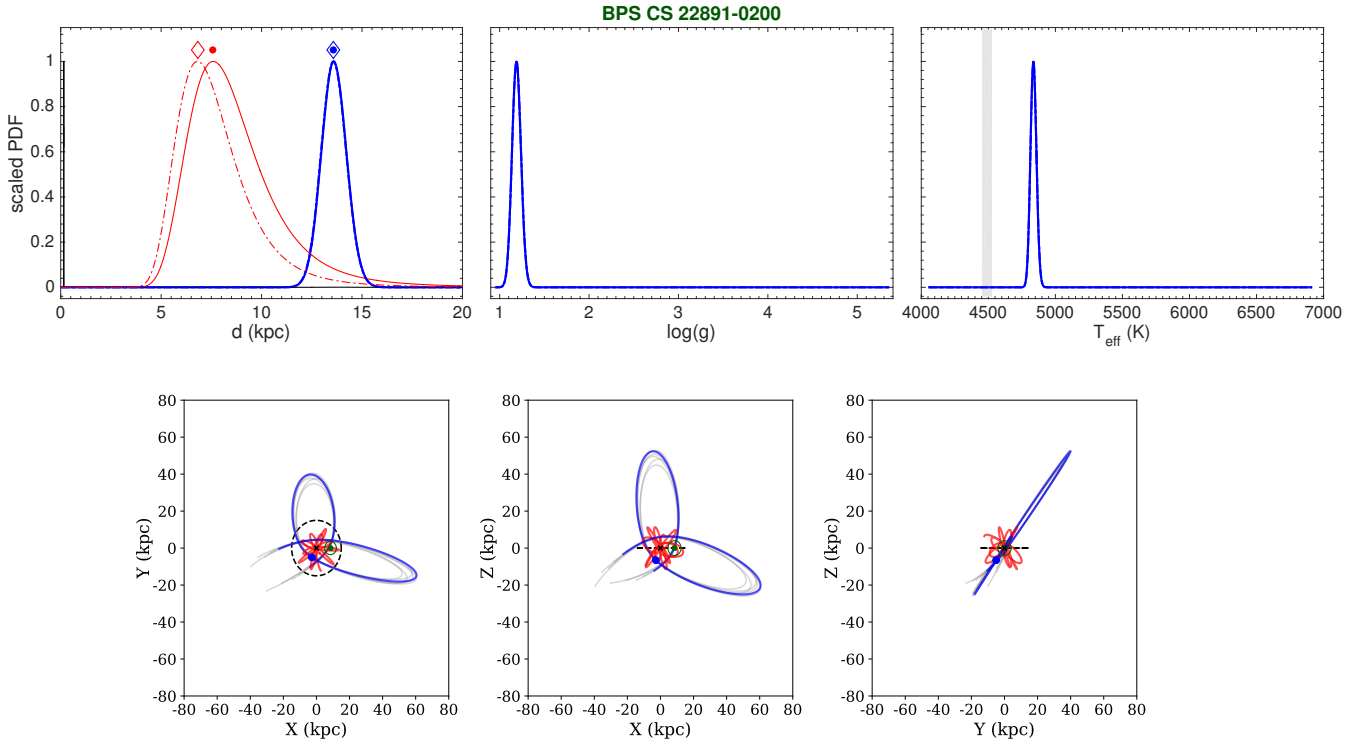


Figure A36. Same as Figure A2, but for BPS CS 22891-0200. The literature value for surface gravity is out of range in the plot. For this star, the orbit inferred from the product between the astrometric likelihood and MW halo prior is shown with the red line.

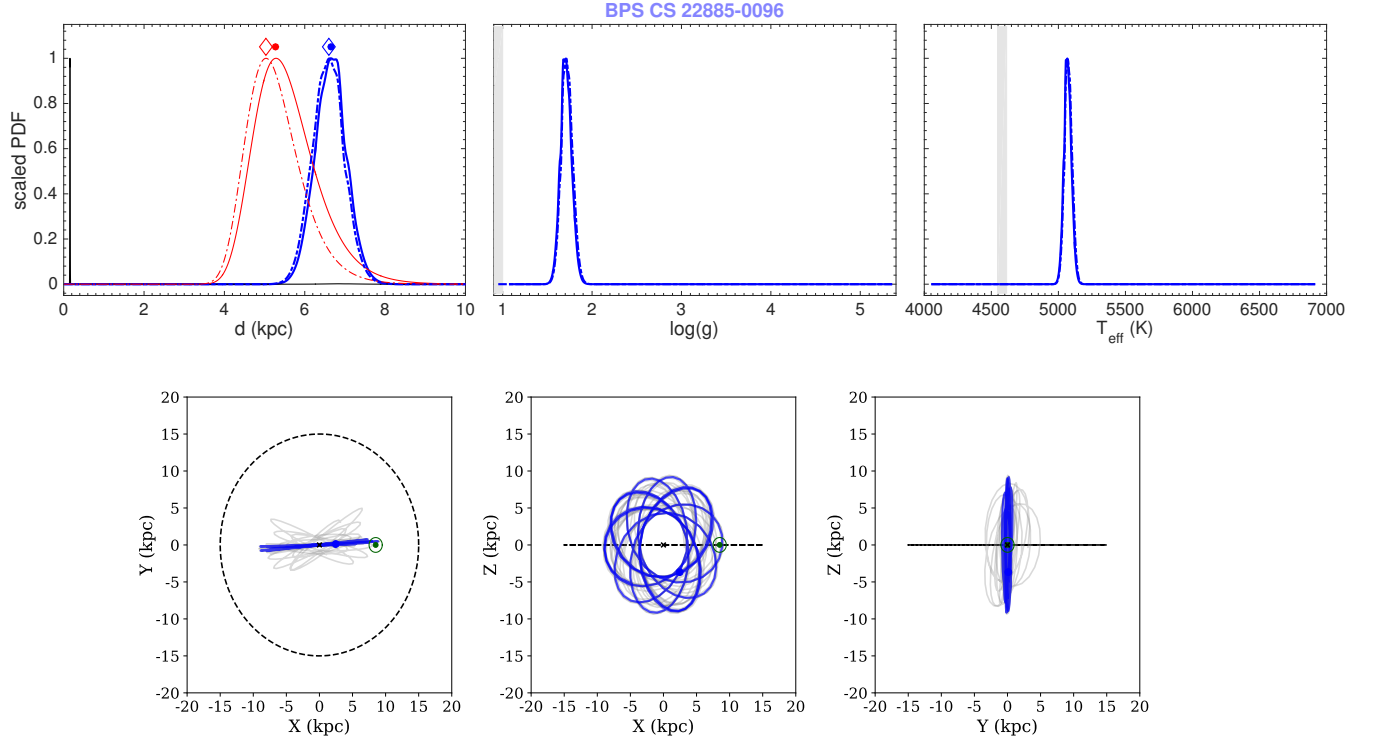


Figure A37. Same as Figure A2, but for BPS CS 22885-0096.

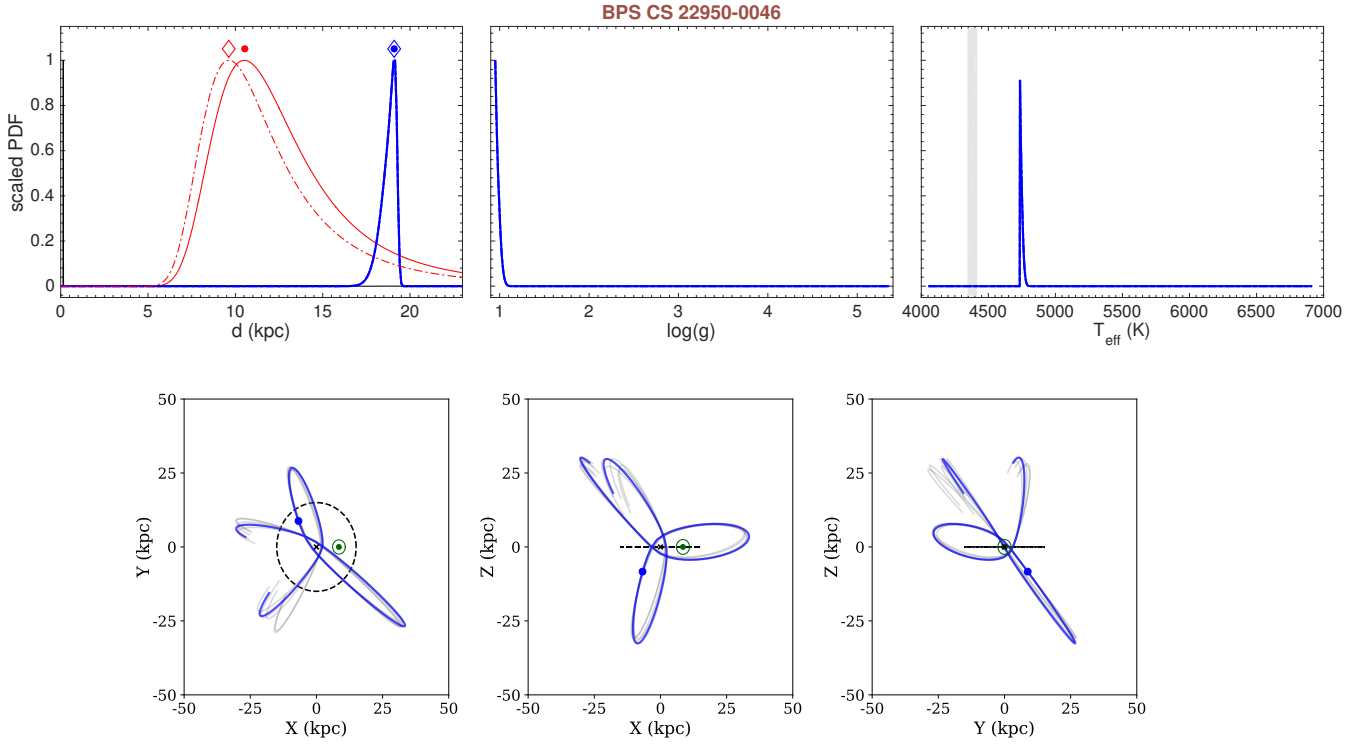


Figure A38. Same as Figure A2, but for BPS CS 22950-0046. The literature value for surface gravity is out of range in the plot.

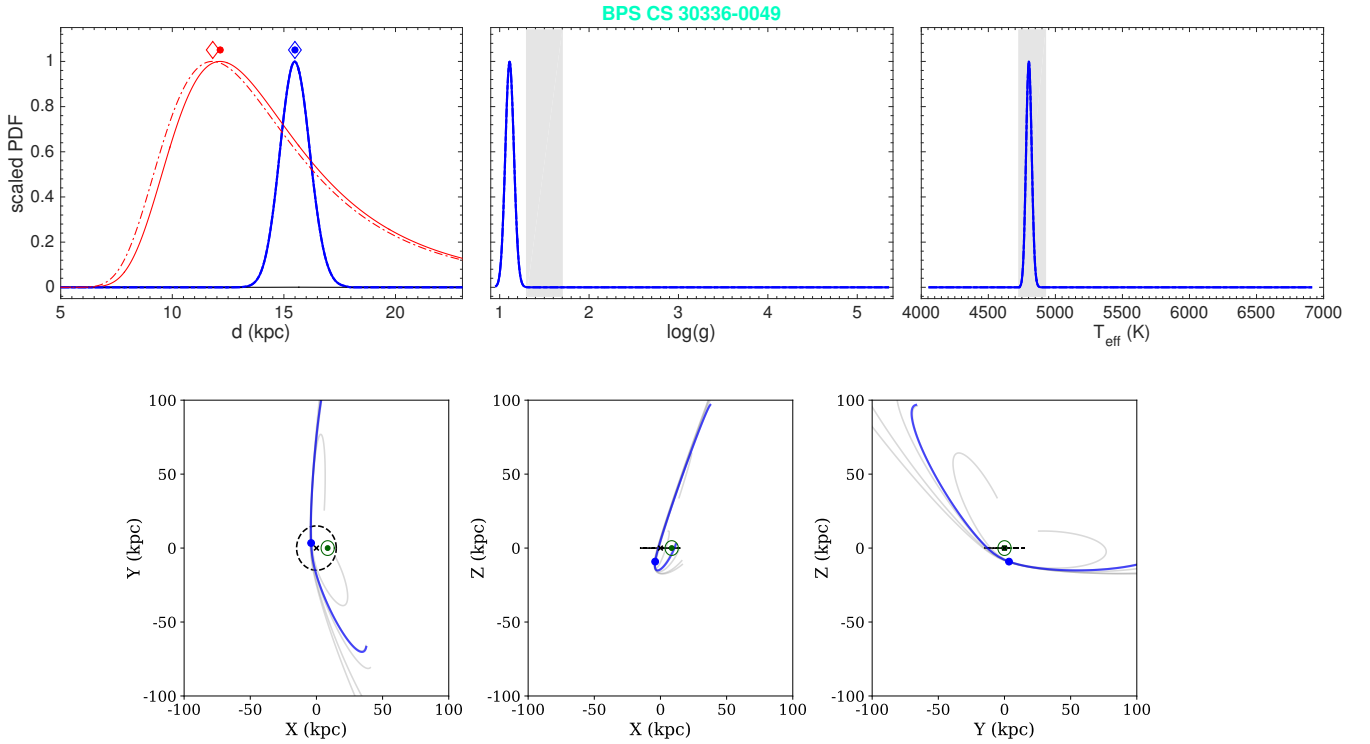


Figure A39. Same as Figure A2, but for BPS CS 30336-0049.

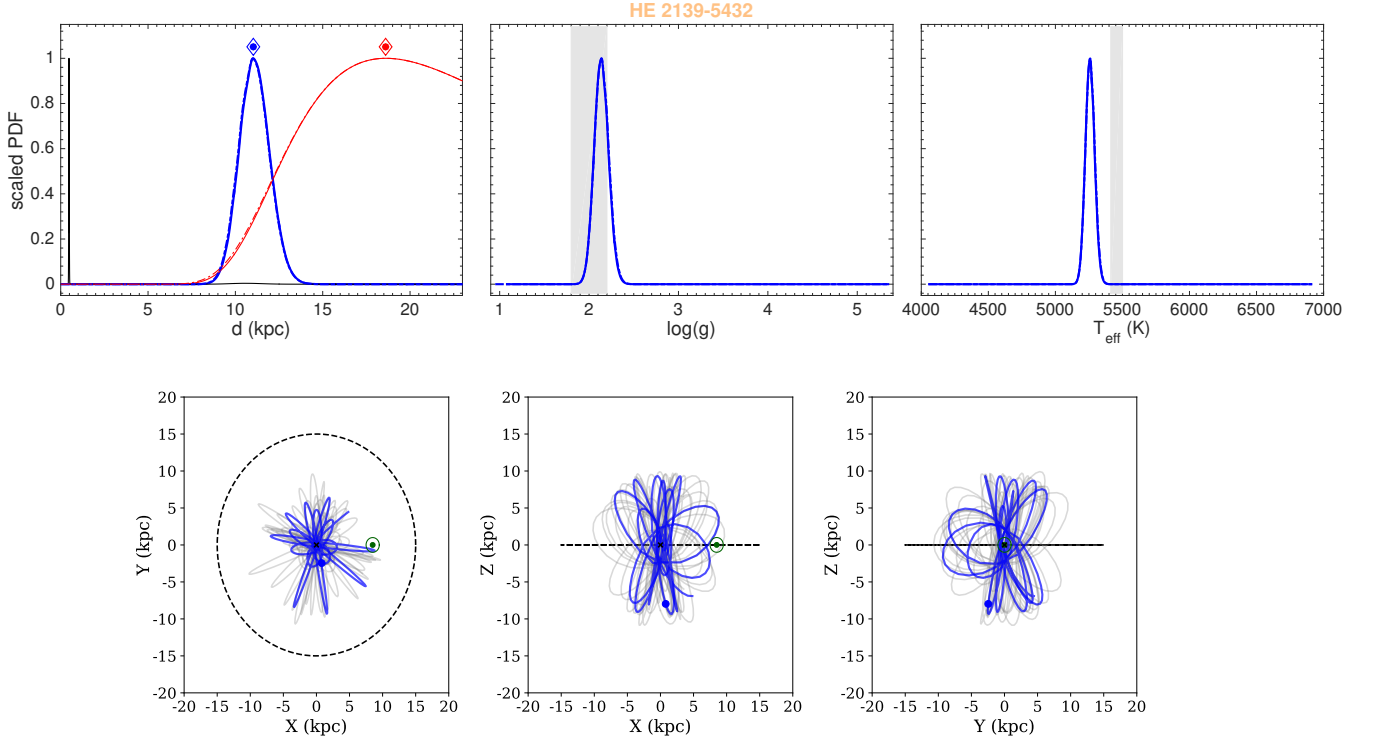


Figure A40. Same as Figure A2, but for HE 2139-5432.

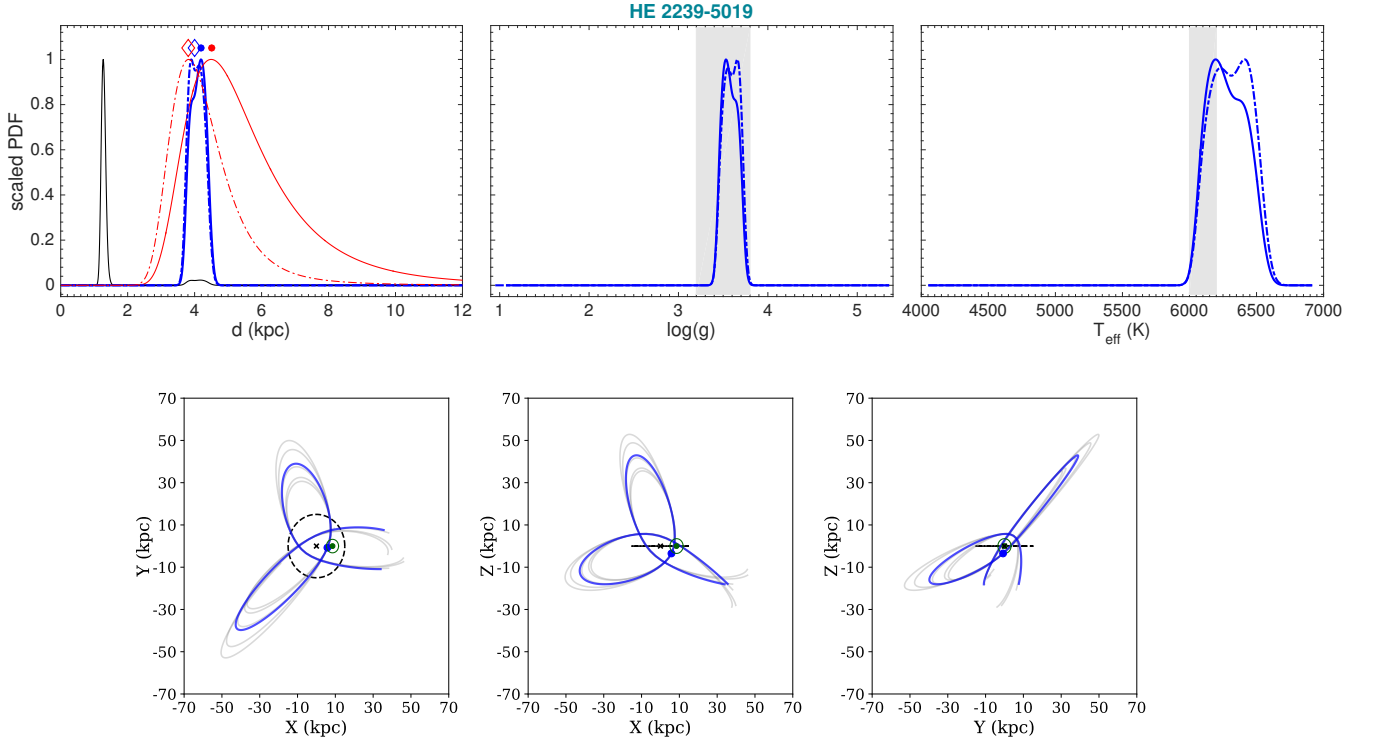


Figure A41. Same as Figure A2, but for HE 2239-5019.

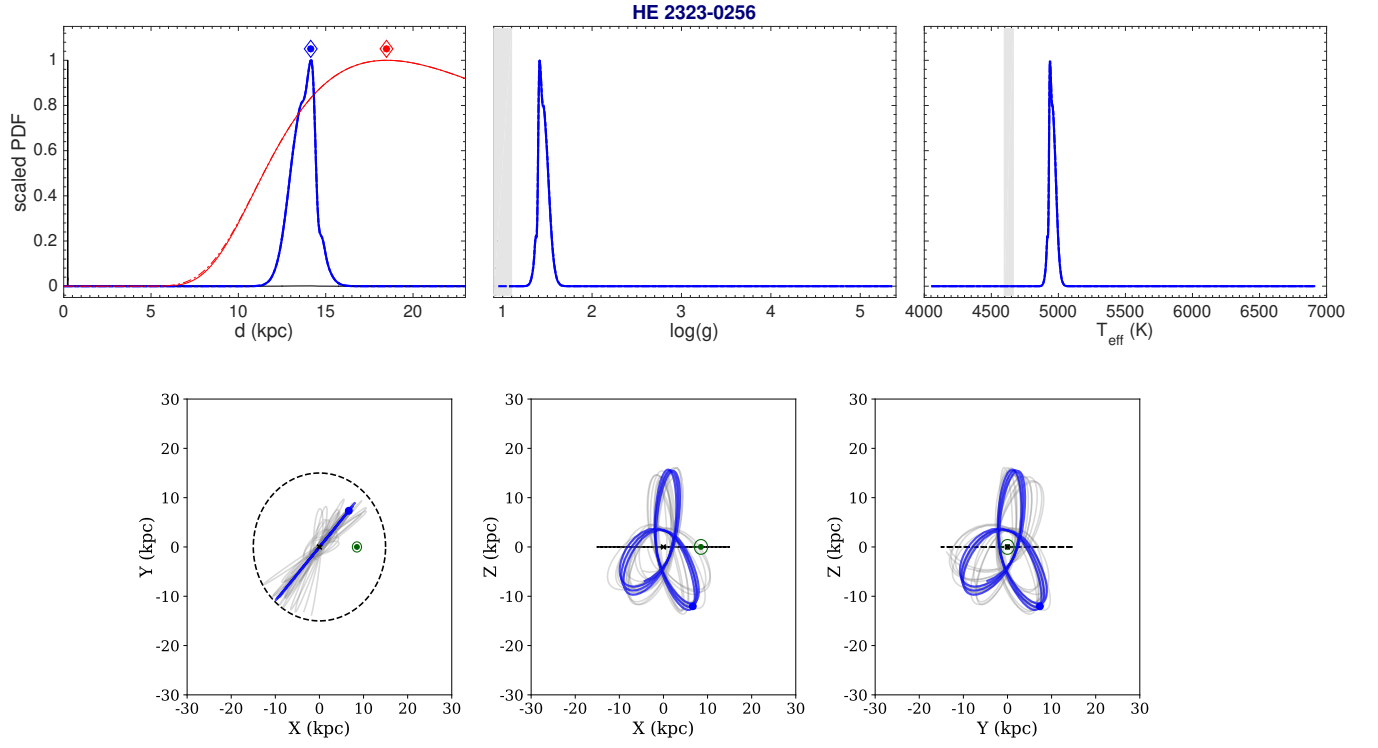


Figure A42. Same as Figure A2, but for HE 2323-0256.

APPENDIX B: COMPARISON WITH VALUES FROM LITERATURE

A global comparison between the stellar parameters inferred in this work and the values found in the literature is reported in the two panels of Figure B1. As we can see, we find a broad agreement for the effective temperature (left panel) and the surface gravity (right panel). Possible systematics are involved both in our method (e.g. $T_{\text{eff}} - \log(g)$ relation in the MESA/MIST isochrones) and the multiple spectroscopic methods used by different authors (e.g. grid based models, synthetic spectra, data-driven analysis etc.).

REFERENCES

- Aguado D. S., Allende Prieto C., González Hernández J. I., Carrera R., Rebolo R., Shetrone M., Lambert D. L., Fernández-Alvar E., 2016, *A&A*, 593, A10
- Aguado D. S., Allende Prieto C., González Hernández J. I., Rebolo R., 2018a, *ApJL*, 854, L34
- Aguado D. S., Allende Prieto C., González Hernández J. I., Rebolo R., Caffau E., 2017a, *A&A*, 604, A9
- Aguado D. S., González Hernández J. I., Allende Prieto C., Rebolo R., 2017b, *A&A*, 605, A40
- , 2018b, *ApJL*, 852, L20
- Allende Prieto C. et al., 2015, *A&A*, 579, A98
- Arentsen A., Starkenburg E., Shetrone M. D., Venn K. A., Depagne É., McConnachie A. W., 2018, *arXiv e-prints*
- Bonifacio P. et al., 2015, *A&A*, 579, A28
- , 2018, *A&A*, 612, A65
- Caffau E. et al., 2012, *A&A*, 542, A51
- , 2013a, *A&A*, 560, A15
- Caffau E. et al., 2011, *Nature*, 477, 67 EP
- Caffau E. et al., 2013b, *A&A*, 560, A71
- , 2016, *A&A*, 595, L6
- Cayrel R. et al., 2004, *A&A*, 416, 1117
- Christlieb N., Gustafsson B., Korn A. J., Barklem P. S., Beers T. C., Bessell M. S., Karlsson T., Mizuno-Wiedner M., 2004, *ApJ*, 603, 708
- Cohen J. G., Christlieb N., McWilliam A., Shectman S., Thompson I., Melendez J., Wisotzki L., Reimers D., 2008, *ApJ*, 672, 320
- Dahn C. C., Liebert J., Kron R. G., Spinrad H., Hintzen P. M., 1977, *ApJ*, 216, 757
- Dearborn D. S. P., Liebert J., Aaronson M., Dahn C. C., Harrington R., Mould J., Greenstein J. L., 1986, *ApJ*, 300, 314
- Frebel A., Chiti A., Ji A. P., Jacobson H. R., Placco V. M., 2015, *ApJL*, 810, L27
- Frebel A., Collet R., Eriksson K., Christlieb N., Aoki W., 2008, *ApJ*, 684, 588
- Hansen T. et al., 2015, *ApJ*, 807, 173
- Ito H., Aoki W., Beers T. C., Tominaga N., Honda S., Carollo D., 2013, *ApJ*, 773, 33
- Lai D. K., Bolte M., Johnson J. A., Lucatello S., Heger A., Woosley S. E., 2008, *ApJ*, 681, 1524
- Li H., Aoki W., Zhao G., Honda S., Christlieb N., Suda T., 2015, *PASJ*, 67, 84
- Meléndez J., Placco V. M., Tucci-Maia M., Ramírez I., Li T. S., Perez G., 2016, *A&A*, 585, L5
- Nordlander T., Amarsi A. M., Lind K., Asplund M., Barklem P. S., Casey A. R., Collet R., Leenaarts J., 2017, *A&A*, 597, A6
- Norris J. E. et al., 2013, *ApJ*, 762, 25
- Norris J. E., Christlieb N., Korn A. J., Eriksson K., Bessell M. S., Beers T. C., Wisotzki L., Reimers D., 2007, *ApJ*, 670, 774
- Placco V. M. et al., 2016, *ApJ*, 833, 21
- Placco V. M., Frebel A., Lee Y. S., Jacobson H. R., Beers T. C., Pena J. M., Chan C., Heger A., 2015, *ApJ*, 809, 136
- Roederer I. U., Preston G. W., Thompson I. B., Shectman S. A., Sneden C., Burley G. S., Kelson D. D., 2014, *The Astronomical Journal*, 147, 136
- Roeser S., Demleitner M., Schilbach E., 2010, *AJ*, 139, 2440
- Schlafman K. C., Thompson I. B., Casey A. R., 2018, *ArXiv e-prints*
- Starkenburg E. et al., 2018, *MNRAS*, 481, 3838
- Yong D. et al., 2013, *ApJ*, 762, 26

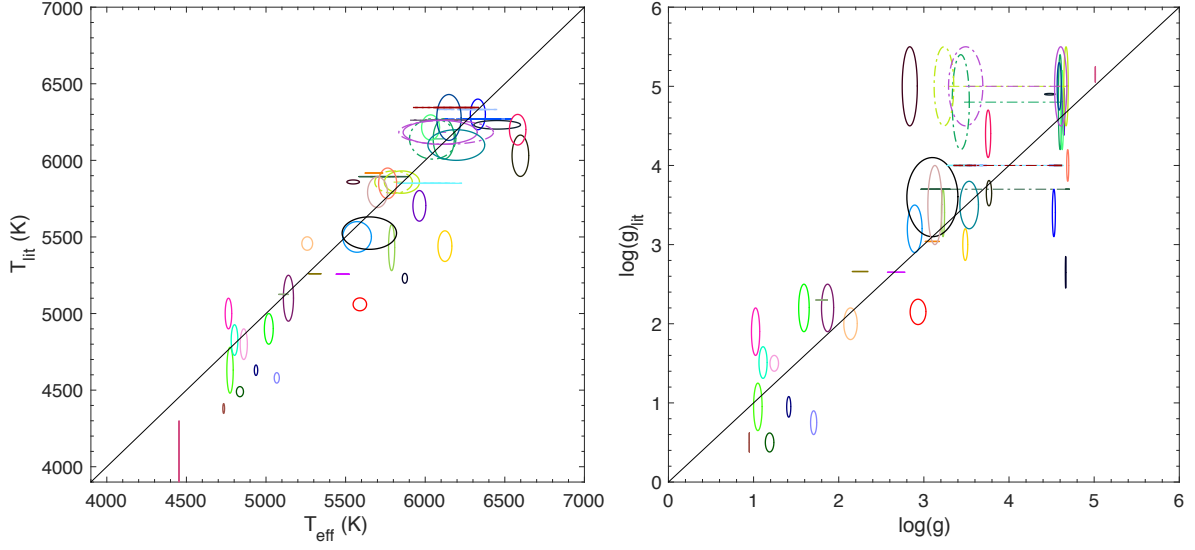


Figure B1. Comparison between inferred effective temperature T_{eff} (left panel), surface gravity $\log(g)$ (right panel) and the values from the literature. The ellipses represent the position of the stars within 1 sigma and the black line corresponds to the 1:1 relation. If the dwarf-giant degeneracy is not broken, the two possible solutions are represented and connected by a dot-dashed line of the same colour code. Each colour represents a star and the colour-code is the same as the colour-code for the markers in Figures 1 - 2 and the panel's titles in Figures A1 - A42. Solutions with integrated probability ($\int_{d-3\sigma}^{d+3\sigma} P(r)dr$) lower than 5% are not shown and solutions with integrated probability in the range [5%, 50%] are shown with dot-dashed ellipses.